Numerical investigation of bubble dynamics at a corner

Wang, Qian; Mahmud, Mehdi; Smith, Warren; Walmsley, Damian

DOI:
10.1063/1.5140740

Numerical investigation of bubble dynamics at a corner

Qianxi Wang (汪前喜)[1*], Mehdi Mahmud[1,2], Jie Cui (崔杰)[3], Warren R. Smith[1] and A. D. Walmsley[4]

[1]School of Mathematics, University of Birmingham, Edgbaston, Birmingham, B15 2TT, UK

[2]College of Science, University of Salahaddin-Erbil, Kurdistan Region, 44001, Iraq

[3]School of Naval Architecture and Ocean Engineering, Jiangsu University of Science and Technology, Zhenjiang, 212003, China

[4]School of Dentistry, College of Medical and Dental Sciences, University of Birmingham, Birmingham, B5 7SA, UK

This paper is concerned with bubble dynamics at a corner formed by two flat rigid boundaries, which is associated with applications in ultrasonic cleaning and cavitation damage. This phenomenon is modelled using the potential flow theory and the boundary integral method. The Green function is obtained to satisfy the impenetrable conditions at the rigid boundaries using the method of images, with the corner angle $\alpha = \pi/k$, where k is a natural number. To evaluate the numerical model, experiments were carried out with a spark-generated bubble in water and recorded by a high-speed camera. The predicted bubble shapes have excellent agreement with experiments. A jet forms towards the end of the collapse, pointing to the corner when initiated at the bisector of the two walls, but pointing to the near wall and inclined to the corner when initiated nearer one of the two walls. The Kelvin impulse theory predicts the jet direction well. As compared to a bubble near a flat wall, the oscillation period and the jet width increase but the jet velocity decreases. The bubble migrates away from the near wall and corner during its expansion and moves back towards them during its collapse, but at much larger speed and amplitude. A velocity stagnation point forms at the start of the collapse and a high-pressure zone is generated at the base of the jet during the late stages of the collapse, which drives the jet and the bubble towards the near wall and corner.

Key words: Bubble dynamics; Bubble Jetting; Boundary Integral Method; Green's function; Method of images.

---

1. Introduction

Bubble dynamics near a rigid boundary are associated with cavitation damage to pumps, turbines and propellers (Blake & Gibson 1987; Brennen 1995; Lauterborn & Kurz 2010). Microbubble dynamics near a boundary subject to an acoustic wave are associated with applications in biomedical ultrasonics (Coussios & Roy 2007; Kim, et al 2009; Curtiss et al. 2013; Brennen 2015; Vyas et al. 2016 2017), and ultrasonic cavitation cleaning (Ohl et al. 2006; Chahine et al. 2016; Rosselló et al. 2018;Yamashita & Ando 2019).

A collapsing bubble migrates to a flat rigid boundary which results in the formation of a high-speed liquid jet on the distal side pointing towards the boundary. The jet pierces the bubble and forms a toroidal bubble. The jet then penetrates the fluid between the bubble and boundary and subsequently impacts on the boundary. This phenomenon has been studied for decades (Lauterborn & Bolle 1975; Vogel, Lauterborn & Timm 1989; Philipp & Lauterborn 1998; Brujan et al. 2002; Lindau & Lauterborn 2003; Brujan et al. 2012; Liu et al. 2016; Supponen et al. 2016, 2017; Lechner et al. 2017). The jet concentrates momentum along its direction and impacts on a small area of the boundary. This concept is believed to be one of the main mechanisms of cleaning or damaging a rigid boundary (Hsiao et al. 2014; Chahine et al. 2016). Another main cause of

cavitation erosion is due to shock waves emitted from the torus ring coming into contact with the boundary (Tomita & Shima 1986; Philipp & Lauterborn 1998; Wang 2014).

Relatively, much less research has been carried out on bubble dynamics near non-flat rigid boundaries. However, geometries in applications are often more complex than just a plane surface. Tomita et al. (2002) studied a bubble collapsing near a curved rigid boundary for an axisymmetric configuration, using high-speed photography as well as the method of images and the boundary integral method (BIM). The curved boundary is prescribed by a family of curves, which are suitable for applying the method of images and conformal mapping. They observed that when a bubble collapses near a curved boundary, the jet velocity may be larger than that near a flat boundary and higher pressures can occur. Brujan et al. (2018) studied the behaviour of a laser-induced cavitation bubble near two perpendicular rigid walls. A liquid jet is formed during bubble collapse pointing mainly to the nearer wall and inclined to the further wall, and the bubble migrates in the direction of the jet.

We will study three-dimensional (3D) bubble dynamics in a corner formed by two flat, rigid boundaries, using the potential flow theory and BIM. This is a basic type of non-flat surface, which often occurs in engineering due to manufacturing procedures and/or practical needs. Kucera and Blake (1990) and Tagawa et al. (2018) provided the Green function for bubble dynamics in a corner having a corner angle $\alpha = \pi/k$, where k is a natural number. The Green function is obtained to satisfy the impenetrable conditions at the flat rigid boundaries using the method of images. Kucera and Blake (1990) obtained the Green function for $\alpha = \pi/4$, and Tagawa et al. (2018) provided the image locations for the corner angle $\alpha = \pi/k$. This paper demonstrates how the images together with the original source are symmetric with respect to both of the walls.

We aim to study the expansion, collapse and migration of the bubble, the behaviour of the jet, and the pressure contours of the flow field. The predicted bubble shapes have excellent agreement with the published experiments for $\alpha = \pi/2$ as well as the experiments performed for electric spark generated bubbles for $\alpha = \pi/4$. A parametric study is carried out in terms of the corner angle and the dimensionless standoff distances of the bubble centre at inception from the two walls.

2. Physical and mathematical modelling

Consider the dynamics of a gas bubble near a corner with an angle α formed by two rigid flat boundaries, to be called wall_1 and wall_2 henceforth, as shown in figure 1. The Cartesian coordinate system $Oxyz$ is set, with the Oxy plane being on the wall_1, the Ozx plane being the symmetry plane of the configuration and the origin at the intersection vertex of the corner.

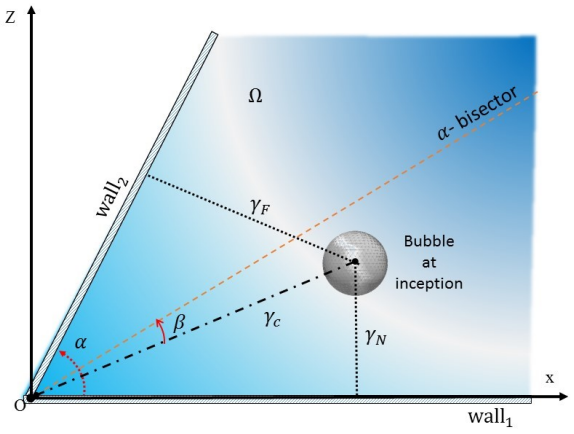

Figure 1: Configuration and coordinate system for bubble dynamics near a corner, with γ_c, γ_N, γ_F, being the dimensionless standoff distances of the bubble centre at inception from the corner, the

near and far wall. The corner angle is α and the eccentricity angle of the initial position of the bubble centre from the α-bisector is β.

The length scale is chosen as the maximum bubble radius R_m and the time reference scale is

$$T = R_m\sqrt{\frac{\rho}{\Delta p}}, \tag{1}$$

where $\Delta p = p_\infty - p_v$, p_∞, p_v and ρ are the ambient pressure, saturated vapour pressure and liquid density, respectively. These values are taken as $p_\infty = 101$ kPa, $p_v = 2.3$ kPa and $\rho = 1000$ kg m^{-3}. Dimensionless variables are used in the remaining text unless stated otherwise.

There are three significant parameters in this phenomenon: the corner angle α, the lean angle from the bisector β of the centre of the initial bubble, and the dimensionless distance, γ_c, from the centre of the initial bubble to the corner vertex,

$$\gamma_c = \frac{d_c}{R_m}. \tag{2}$$

As the problem is symmetric in terms of β, we only consider $\beta \in [0,\ \alpha/2]$. The dimensionless standoff distances γ_N and γ_F from the centre of the initial bubble to the near and far walls are

$$\gamma_N = \gamma_c \sin\left(\frac{\alpha}{2} - \beta\right), \qquad \gamma_F = \gamma_c \sin\left(\frac{\alpha}{2} + \beta\right). \tag{3}$$

The flow is assumed to be incompressible, inviscid and irrotational. The fluid velocity $\boldsymbol{v}$ thus has a potential φ, $\boldsymbol{v} = \nabla\varphi$, satisfying Laplace's equation,

$$\nabla^2\varphi = 0. \tag{4a}$$

The viscous effects of the liquid flow are neglected here since inertial effects are usually dominant for bubble dynamics (Manmi et al. 2017). The compressible effects are only essential during a short period at the end of the collapse (Wang & Blake 2010, 2011; Wang 2016).

The kinematic boundary conditions on the two walls, wall$_1$, wall$_2$, the bubble surface S_B and at the far field are as follows

$$\frac{\partial\varphi}{\partial n} = 0 \quad \text{on} \quad \text{wall}_1, \text{wall}_2, \tag{4b}$$

$$\frac{D\mathbf{r}}{Dt} = \nabla\varphi \quad \text{on} \quad S_B, \tag{4c}$$

$$\nabla\varphi \to 0 \text{ as } r \to \infty, \tag{4d}$$

where $\boldsymbol{r}$ is the position vector of the boundary, $\boldsymbol{n}$ is normal on the boundary surface, D/Dt denotes the material derivative, and r is the radial distance. The impermeable boundary condition on the rigid boundaries is (4b) and (4c) requires a material point on the bubble surface to remain there.

Assuming that the gas-bubble is under an adiabatic process, its dimensional pressure p_B satisfies

$$p_B(t) = p_v + p_{g0}\left(\frac{V_0}{V}\right)^\kappa, \tag{5}$$

where p_{g0} is the initial pressure of the bubble gas, V_0 and V are the initial and transient bubble volumes, and κ is the polytropic index of the bubble gas. Additionally, heat and mass transfer across the bubble surface can be included (Szeri et al. 2003), but are neglected here.

The dynamic boundary condition on the bubble surface S_B requires that the pressure difference across the surface is equal to the Laplace pressure, which can be written as follows by using the Bernoulli equation (Manmi & Wang 2017)

$$\frac{d\varphi}{dt} = 1 + \frac{1}{2}\left|\nabla\varphi\right|^2 - \delta^2 z - \varepsilon\left(\frac{V_0}{V}\right)^{\kappa} + \frac{r_c}{We} - \frac{2(1+C)}{Re}\frac{\partial^2\varphi}{\partial n^2} \text{ on } S_B, \tag{6}$$

where $We = R_m \Delta p/\sigma$ is the Weber number, $\delta = \sqrt{\rho g R_m / p_\infty}$ is the buoyancy parameter, $\varepsilon = p_{g0} / \Delta p$ is dimensionless initial pressure inside the bubble and r_c is the radius of curvature of the bubble surface. The cases considered correspond to small bubbles, therefore the buoyancy effect is negligible, i.e. $\delta = 0$, unless explicitly stated otherwise. Buoyancy effects are essential for large bubbles (Wang 1998, 2004).

The last term in (6) is associated with the viscous effects, where the Reynolds number Re is defined as $Re = R_0\sqrt{\Delta p\ \rho}\ /\ \mu$, $\boldsymbol{n}$ the unit outward normal at the bubble surface S_B directed from liquid to gas and C is determined as following (Manmi & Wang 2017)

$$C = \frac{\int_{S_B} \nabla\phi \cdot \frac{\partial \nabla\phi}{\partial n} dS}{\int_{S_B} \frac{\partial\phi}{\partial n}\frac{\partial^2\phi}{\partial n^2} dS} - 1. \tag{7}$$

Viscous fluid dynamics can be described approximately by potential flows when the vorticity is small or is confined to a narrow layer near the boundary (Joseph & Wang 2004; Joseph et al. 2007). It is particularly useful for a gas–liquid two-phase flow with an interface.

For a bubble subject to an ultrasonic wave, an incident wave should be incorporated into the model by adding the acoustic pressure in (6) (Wang et al 2014). Ultransonic wave effects can cause nonspherical collapse and formation of bubble jetting (Rosselló et al. 2018).

3. Boundary integral method

In this section, we describe the BIM, the Kelvin impulse theory and the calculation of the velocity and pressure field in the flow domain.

3.1 Method of images

Using Green's second theorem, the potential can be expressed as the integral over the bubble surface

$$c(\boldsymbol{r},t)\varphi(\boldsymbol{r},t) = \int_{S_B}\left(\frac{\partial\varphi(\boldsymbol{q},t)}{\partial n}G(\boldsymbol{r},\boldsymbol{q}) - \varphi(\boldsymbol{q},t)\frac{\partial G(\boldsymbol{r},\boldsymbol{q})}{\partial n}\right)dS(\boldsymbol{q}), \tag{8}$$

where $c(\boldsymbol{r}, t)$ is the solid angle of bubble surface at the point $\boldsymbol{r}$. Green's function $G(\boldsymbol{r}, \boldsymbol{q})$ for Laplace's equation satisfies the impenetrable boundary conditions at the two walls.

As the corner angle $\alpha = \pi/k$, in which k is a natural number, the Green function is given by

$$G(\boldsymbol{r},\boldsymbol{q}) = \sum_{j=0}^{2k-1}\frac{1}{|\boldsymbol{r}-\boldsymbol{q}_j|}, \tag{9}$$

where $\boldsymbol{q}_0 = \boldsymbol{q}$ is the source point and $\boldsymbol{q}_j$, $j = 1, 2, \ldots, 2k-1$ are $2k$-1 images of $\boldsymbol{q}_0$ in the two walls. The images were provided by Kucera and Blake (1990) and Tagawa et al. (2018). We provide a proof as follows.

Let the source point $\boldsymbol{q}_0$: (x_0, y_0, z_0) make an angle $\theta_0 = \theta_a$ with wall$_1$ and its successive images $\boldsymbol{q}_j$ = (x_j, y_0, z_j), which make an angle θ_j with wall$_1$. The images lie on a circle with centre at (0, y_0, 0) and a radius $r_q = \sqrt{x_0^2 + z_0^2}$. Figure 2 illustrates the images when a bubble is located between two walls inclined at an angle $\alpha = \pi/2$.

The angles of $\theta_j, j = 0, 1, 2, \ldots, 2k\text{-}1$, can be divided into two groups as follows

$$\left\{-\frac{2l\pi}{k}-\theta_a, \frac{2l\pi}{k}+\theta_a\right\},\ l = 0,\ 1,\ 2,\ \ldots, k-1. \tag{10}$$

The source and images are thus symmetric to wall$_1$. Their angles relative to wall$_2$ are $\Theta_j = \theta_j - \pi/k$ whose corresponding groups are

$$\left\{-\frac{(2l+1)\pi}{k}-\theta_a, \frac{(2l-1)\pi}{k}+\theta_a\right\}, l = 0,\ 1,\ 2,\ \ldots, k-1. \tag{11}$$

Notice the last angle in the first group is $-(2k-1)\pi/k-\theta_a = -2\pi+\pi/k-\theta_a$, which is identical to $\pi/k-\theta_a$. Upon moving this last element from the first group to the first element, we have

$$\left\{-\frac{(2l-1)\pi}{k}-\theta_a, \frac{(2l-1)\pi}{k}+\theta_a\right\}, l = 0,\ 1,\ 2,\ \ldots,\ k\text{-}1. \tag{12}$$

Therefore, the source and the images are also symmetric to wall$_2$.

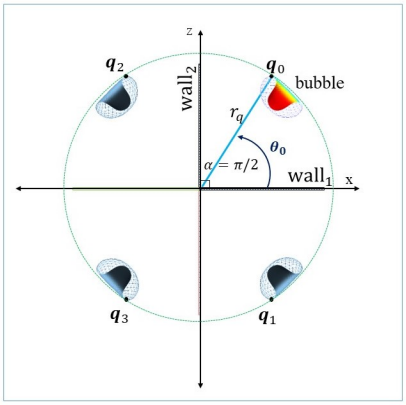

Figure 2. The images for a source point $\boldsymbol{q}_0$ which makes angle θ_0 with wall$_1$ for $\alpha = \pi/2$.

The BIM model is grid-free in the flow domain and computationally efficient and is thus widely used in the field of bubble dynamics. Linear planar triangular elements are used in the present BIM model. At each time step, we have a known bubble surface and known potential distribution on the surface. With this information, the tangential velocity on the bubble surface can be calculated from the gradient of the potential at the surface. The normal velocity on the bubble surface is obtained after solving the boundary integral equation (8). The bubble surface and potential distribution on the bubble surface are updated by performing the Lagrangian time integration to (2.4c, 2.6). This is obtained by using a second-order Runge-Kutta scheme, and an interpolated polynomial scheme coupled with the moving least square method. A variable time step is chosen for accuracy and efficiency, in such a way that the maximum change of the potential in each time step is restricted by a constant (Blake et al. 1986, 1987). A high-quality surface mesh is maintained by implementing a hybrid approach of the Lagrangian method and elastic mesh technique. The details of the numerical model using the BIM model for this problem can be found in (Wang & Manmi 2014, 2015; Zhang & Liu 2015).

3.2 Kelvin impulse theory

The Kelvin impulse $\boldsymbol{I}$ of a bubble is defined as

$$\boldsymbol{I} = \int_{S_B} \varphi \boldsymbol{n}\, dS\,. \tag{13}$$

The Kelvin impulse corresponds to the apparent inertia of the bubble and its direction indicates the directions of the bubble migration and bubble jet (Blake 1988; Blake et al. 2015).

If the bubble is taken a sufficient distance away from the boundary, it may be represented approximately by a time-varying point source. For a bubble at a corner with an angle of $\alpha = \pi/k$, where k is a natural number, the potential can be approximated by

$$\varphi(\boldsymbol{r},t) = \frac{-m(t)}{4\pi}\sum_{j=0}^{2k-1}\frac{1}{|\boldsymbol{r}-\boldsymbol{q}_j|}, \tag{14}$$

where $m(t)$ is the source strength given by $4\pi R^2(t)\,dR(t)/dt$, where $R(t)$ is the transient radius of the bubble. In this section, $\boldsymbol{q}_0$ denotes the initial bubble centroid and $\boldsymbol{q}_j$ for $j \geq 1$ denotes its images in the two walls.

The potential $\varphi(\boldsymbol{r}, t)$ in (3.7) can be rewritten as

$$\varphi(\boldsymbol{r},t) = \frac{-m(t)}{4\pi|\boldsymbol{r}-\boldsymbol{q}_0|} + \Phi(\boldsymbol{r},t), \qquad \Phi(\boldsymbol{r},t) = \frac{-m(t)}{4\pi}\sum_{j=1}^{2k-1}\frac{1}{|\boldsymbol{r}-\boldsymbol{q}_j|}. \tag{15}$$

Utilising this notation, the Kelvin impulse can be calculated as follows (Best & Blake 1994)

$$\boldsymbol{I} = \int_0^t \boldsymbol{F}(t)dt, \tag{16}$$

where

$$\boldsymbol{F}(t) = -m(t)\nabla\Phi(\boldsymbol{r}_s,t) = \frac{m^2(t)}{4\pi}\sum_{j=1}^{2k-1}\nabla\left(\frac{1}{|\boldsymbol{r}-\boldsymbol{q}_j|}\right)\Bigg|_{\boldsymbol{r}=\boldsymbol{q}_0} = -\frac{m^2(t)}{4\pi}\sum_{j=1}^{2k-1}\frac{\boldsymbol{q}_0-\boldsymbol{q}_j}{|\boldsymbol{q}_0-\boldsymbol{q}_j|^3}. \tag{17}$$

Substituting (17) into (16), we have

$$\boldsymbol{I}(t) = -\frac{1}{4\pi}\int_0^t m^2(t)\,dt\sum_{j=1}^{2k-1}\frac{\boldsymbol{q}_0-\boldsymbol{q}_j}{|\boldsymbol{q}_0-\boldsymbol{q}_j|^3}. \tag{18}$$

The Kelvin impulse is determined by the positions of the initial bubble and its images in the two walls (or the corner angle α). Tagawa et al. (2018) obtained the induced velocity at the bubble centroid using the method of images and complex functions via a two-dimensional analysis, which is in the same direction as the Kelvin impulse (18).

The Rayleigh bubble solution for $m(t)$ is (Blake et al. 1986),

$$m^2(t) = \frac{32\pi^2}{2}R(1-R^3). \tag{19}$$

For a Rayleigh bubble, we can calculate the Kelvin impulse at the end of collapse $T_c \approx 1.83$ as follows

$$\boldsymbol{I}(T_c) = -\frac{8\sqrt{6}\pi}{9}B\left(\tfrac{7}{6},\tfrac{3}{2}\right)\sum_{j=1}^{2k-1}\frac{\boldsymbol{q}_0-\boldsymbol{q}_j}{|\boldsymbol{q}_0-\boldsymbol{q}_j|^3}, \tag{20}$$

where $B(z,$ w) is the beta function (see Abramowitz & Stegun (1965)).

3.3 Calculation of velocity and pressure in the flow domain

The velocity $\nabla\varphi$ can be calculated using the finite difference method with the potential calculated from the BIM. The pressure distribution can be calculated using the Bernoulli equation,

$$p = 1 - \frac{\partial\varphi}{\partial t} - \frac{1}{2}|\nabla\varphi|^2 - \delta^2 z. \tag{21}$$

However, to calculate $\dot{\varphi} = \partial\varphi/\partial t$ using the finite difference method often results in unacceptable errors, due to the very small time-steps usually used for simulating a violent collapsing bubble. We calculate $\dot{\varphi} = \partial\varphi/\partial t$ using the BIM model following Tanizawa (1995) and Wu (1998).

The boundary volume problem for $\dot{\varphi}$ can be obtained from (2.4a, b, d) as follows:

$$\nabla^2\dot{\varphi}=0, \tag{22a}$$

$$\frac{\partial\dot{\varphi}}{\partial n}=0 \quad \text{on } \text{wall}_1, \text{wall}_2, \tag{22b}$$

$$\nabla\dot{\varphi}\to 0 \text{ as } r\to\infty. \tag{22c}$$

As such, $\dot{\varphi}$ satisfies the same boundary integral equation on the bubble surface as φ as follows

$$c(\boldsymbol{r},t)\dot{\varphi}(\boldsymbol{r},t)=\int_{S_B}\left(\frac{\partial\dot{\varphi}(\boldsymbol{q},t)}{\partial n}G(\boldsymbol{r},\boldsymbol{q})-\dot{\varphi}(\boldsymbol{q},t)\frac{\partial G(\boldsymbol{r},\boldsymbol{q})}{\partial n}\right)dS(\boldsymbol{q}), \tag{23}$$

where $G(\boldsymbol{r}, \boldsymbol{q})$ is the same Green's function given in (3.2). $\dot{\varphi}$ on S_B is obtained from the dynamic boundary condition

$$\dot{\varphi}=1-\frac{1}{2}|\nabla\varphi|^2-\delta^2 z-\varepsilon\left(\frac{V_0}{V}\right)^{\kappa}+\frac{r_c}{We} \text{ on } S_B. \tag{24}$$

On the bubble surface S_B, $\partial\dot{\varphi}/\partial n$ can thus be calculated using the BIM (8). In the flow field, $\dot{\varphi}(\mathbf{r}, t)$ is then calculated using (23).

To verify the results, the numerical model is compared with the Rayleigh-Plesset equation (RPE) for a spherical bubble in an unbounded liquid. The pressure $p(\mathbf{r}, t)$ from the spherical bubble theory is given as follows, in a coordinate system with the origin at the centre of the bubble

$$p(\mathbf{r},t)=1+\frac{R^2(t)}{r}\ddot{R}(t)+2\left(\frac{R(t)}{r}-\frac{1}{4}\frac{R^4(t)}{r^4}\right)\dot{R}^2. \tag{25}$$

Figure 3 compares the BIM and the spherical bubble theory for the time histories of the pressure for two different field points, with radial distances from the bubble centre at r = 1.5 and r = 5, in figure 3(a) and 3(b) respectively. The BIM results have excellent agreement with that of the spherical bubble theory.

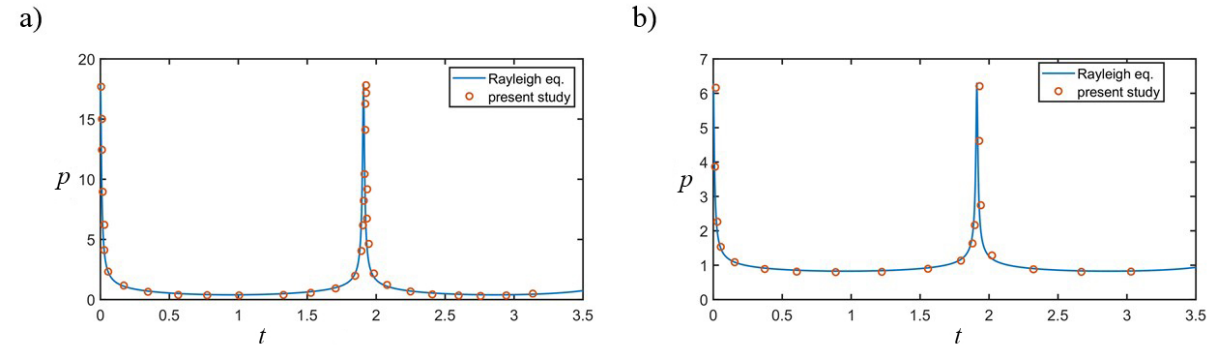

Figure 3. Comparison of the pressure for RPE and BIM for a spherical bubble in an unbounded liquid at a field point, with radial distances from the bubble centre at (a) r = 1.5 and (b) r = 5. The remaining parameters are R_m = 0.8mm, ε = 200, δ = 0.0089, We = 1084 and κ = 1.4.

We next compare the present results with the pressure calculated with an axisymmetric BIM by Li et al. (2016). It is for a bubble with R_m =16.6mm above a rigid wall, with the initial standoff distance γ_W = 0.99, ε = 50, δ = 0.04, We=2250 and κ = 1.4. The present 3D BIM in figure 4(a) agrees well with the axisymmetric BIM (Li et al. 2016) shown in figure 4(b) for the pressure contours, velocity field, bubble shape and jet shape immediately before jet impact.

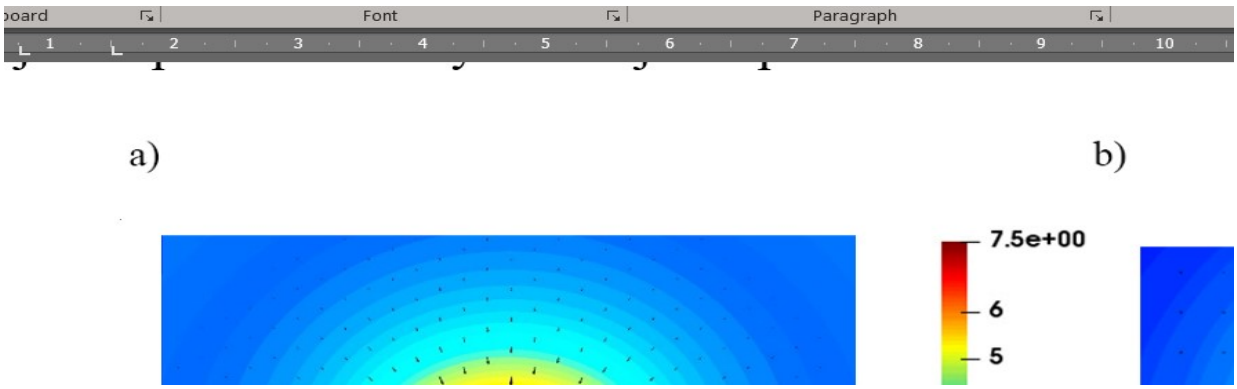

Figure 4. Comparison between the velocity field and pressure distributions of the (a) 3D-BIM model (present study) and (b) axisymmetric BIM (Li et al. 2016), for a bubble near a wall with γ_W = 0.99, and at t = 2.32. The remaining parameters are R_m = 16.6mm, ε = 50, δ = 0.04, We = 22500, δ = 0.04 and κ = 1.4.

4. Validation of the numerical model

4.1 *Comparison with experiments*

To evaluate the BIM model, we compare the computational results with experimental images. The first case is for a laser beam generated bubble having a maximum radius R_m = 0.85mm at a right-angled corner for $\alpha = \pi/2$, $\beta = 0.1$, $\gamma_N = 1.08$, and $\gamma_F = 0.88$ (Brujan et al. 2018). The corresponding dimensionless distance of the bubble centre at the inception form the near and far walls are γ_N = 0.88 and γ_F = 1.08. As shown in figure 5, during the early stages of the expansion (frame 1), the bubble remains spherical except its surface facing the near wall is retarded by the wall. At the end of the expansion (frame 3), the parts of the bubble surface facing two walls are flattened by the walls, with the greater flattening by the near wall, while the distal part opposite to the corner remains spherical. The bubble collapses from the distal side, with the near wall sides kept in contact with the wall (frames 3-6). Towards the end of the collapse, a wide jet forms on the distal side which points to the corner (frames 5-6). All the features are reproduced by the computations and the bubble shapes obtained from the computations are in very good agreement with the experiments, except that the bubble jet is not visible in the experiments due to the opaqueness of the bubble.

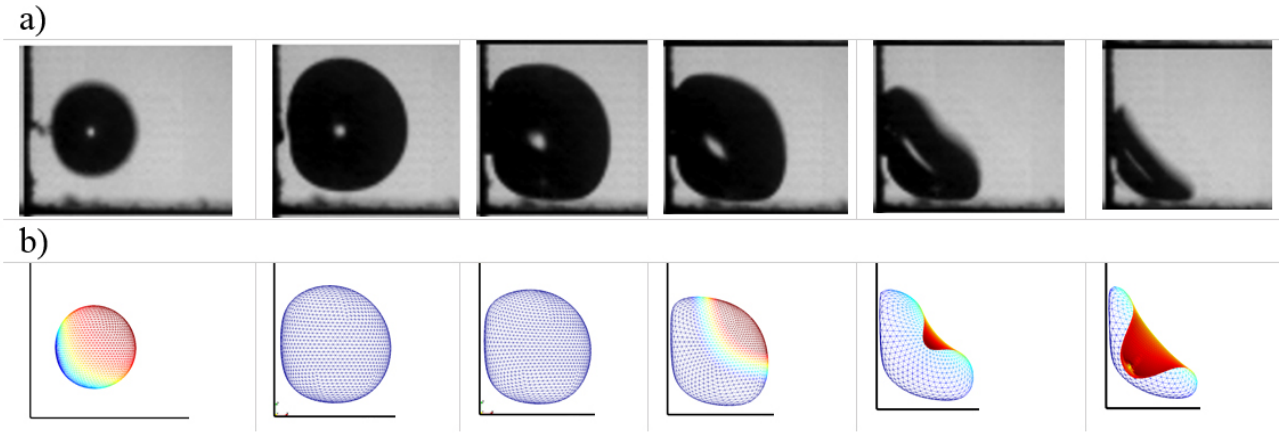

Figure 5. Comparison between (a) experimental (Brujan et al. 2018) and (b) BIM results characterized by $\alpha = \pi/2$, $\beta = 0.1$, $\gamma_N = 1.08$, and $\gamma_F = 0.88$, R_m = 0.85mm, $\varepsilon = 100$, $We = 1152$, δ = 0.009 and $\kappa = 1.4$. The dimensionless times are t = 0.2, 0.9, 1.37, 2.1, 2.52, and 2.683, respectively.

The second case is for a bubble initiated at the bisector of an acute corner for $\alpha = \pi/4$, $\beta = 0$ and γ_c = 1.45. The experiments were carried out with a spark-generated bubble in water and recorded by a high-speed camera. Experiments are performed in a cubic glass tank with 0.5 m side length filled with tap water to a depth of 0.4 m. A corner is formed by two transparent rectangular fiberglass walls with a thickness of 4.5 mm; the joined sides being 210 mm and the other side 150 mm. The two walls are inserted from the top of the glass tank using adjustable positioners. The water tank is illuminated by a 2 kW spot light opposite to the camera through a diffuser (matte glass). Images of bubbles are recorded by a VRI-Phantom V611 high-speed camera working at 20,000 frames per second with an exposure time of 140,000 ns. The interval between two image frames is 144.93 μs, which is small compared to the period of bubble oscillation (about 6 ms). For illumination, a flash lamp with a 500 ms flash duration is used which covers the most relevant part of the first two cycles of oscillation. The timing of the photography is adjusted with an electronic delay circuit.

The maximum bubble radius is about R_m = 13.5mm. This is associated with $\gamma_N = \gamma_F = 1.03$. Large parts of the bubble surface facing two walls are flattened by the walls at the end of the expansion (frame 2) as shown in figure 6. During collapse (frames 3-7), the parts of the bubble

surface facing the two walls are kept in contact with the walls, the distal side opposite to the corner collapses faster than the side facing the corner, a jet forms pointing towards the corner in the late stage of the collapse (frames 6 and 7). Again, the computations agree well with the experiment for this case.

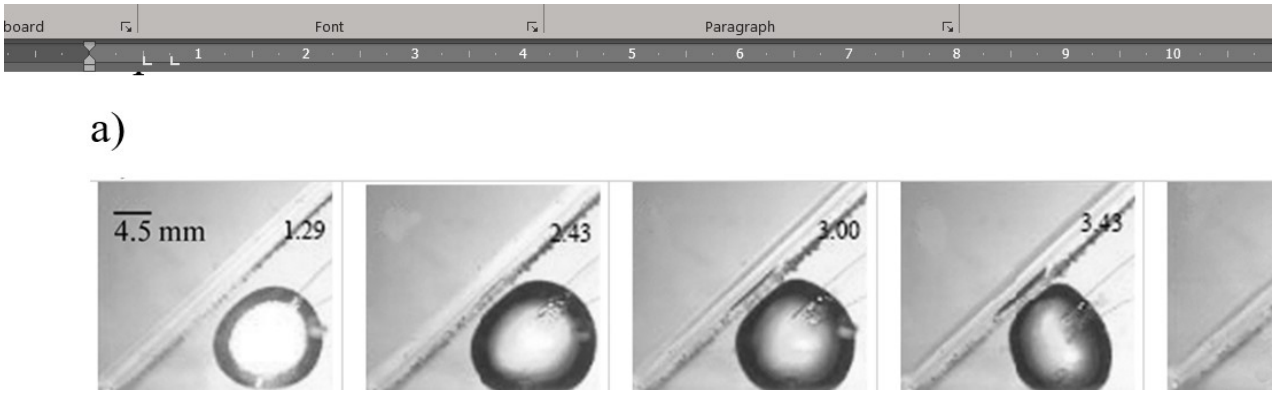

Figure 6. Comparison between (a) experimental and (b) BIM results characterized by $\alpha = \pi/4$, $\beta = 0$, $\gamma_c = 1.45$, $R_m = 13.5$mm, $\varepsilon = 100$, $We = 1886$, $\delta = 0.036$ and $\kappa = 1.4$. The dimensionless times are t =0.96, 1.813, 2.23, 2.55, 2.76, 2.99, and 3.305, respectively.

4.2 *Convergence tests*

To analyze the convergence of the BIM modelling, convergence tests were performed for the case for $\alpha = \pi/2$, $\beta = 0.1$, $\gamma_c = 2.12$ and $R_m = 0.8$mm. Various numbers of the elements were used on the bubble surface, M = 720, 980, 1280 and 2000. Figures 7(a) and 7(b) show the results of the jet velocity v_{jet} and the equivalent bubble radius $R_{eq} = \left(3V/(4\pi)\right)^{1/3}$. Both results converge well with the surface element number M as $M \geq 980$. Figure 7(c) compares the bubble shapes immediately before jet impacting on the opposite bubble surface for various values of M. It shows that the bubble shape for M = 1280 agrees well with that for M = 2000. As such, all the remaining calculations in this study were performed for M = 1280.

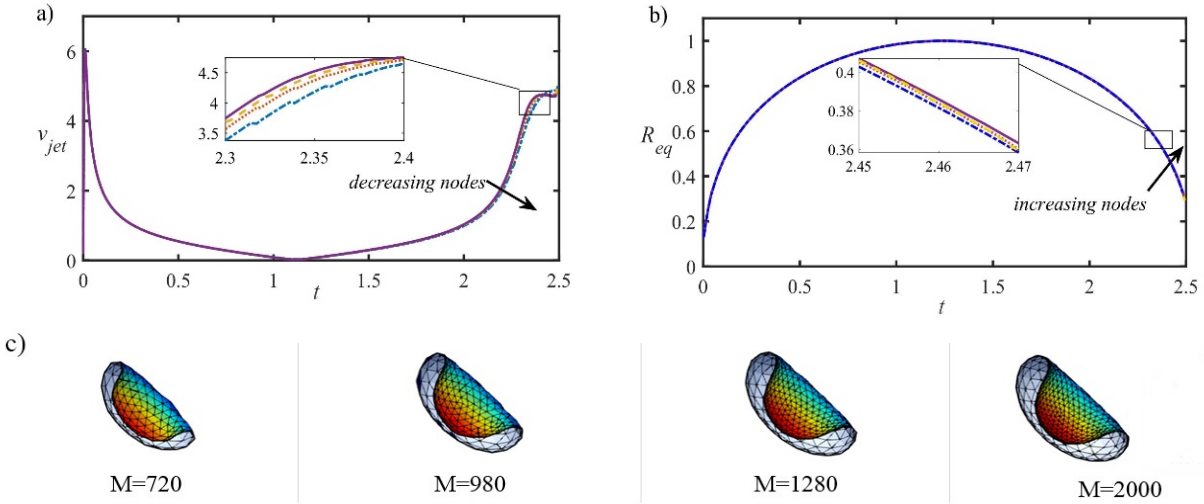

Figure 7. Convergence tests for the BIM modelling in terms of (a) time history of the jet velocity, (b) equivalent bubble radius, and (c) bubble shapes immediately before jet impact for $\alpha = \pi/2$, $\beta = 0$, $\gamma_c = 2.12$, $We = 1084$ and $R_m = 0.8$mm, $\kappa = 1.4$, $\delta = 0.0089$ for various bubble surface elements M = 720, 980, 1280 and 2000.

5. Numerical results

5.1 *Symmetric cases* ($\beta = 0$)

We firstly consider symmetric cases for bubbles initiated at the bisector of the corner for $\beta = 0$. Figure 8 displays bubble dynamics near a right-angled corner $\alpha = \pi/2$ at various standoff distances from the two walls for $\gamma_N = \gamma_F = \gamma = 1, 2, 3, 4, 5, 6$. Each row in figure 8(a) illustrates the bubble shapes at the inception of the bubble, the maximum volume, jet formation, and jet impact on the opposite bubble surface. The bubble expands approximately spherically (frame 1), except for $\gamma = 1$ for which the bubble surfaces facing the two walls are compressed by the walls (frame 1). During the latter stages of the collapse, the bubble becomes oblate along the bisector direction, the far side of the bubble opposite to the corner becomes noticeably flattened and a high-speed liquid jet forms pointing to the corner (frames 2 and 3). As the bubble is initiated closer to the corner, the bubble volumes at the start of jet formation and jet impact increase and the width of the jet increases. The start of jet formation occurs at the moment when the far side becomes flattened.

The Bjerknes forces are forces on bubbles due to pressure. The primary Bjerknes forces are due to an external pressure field, and the secondary Bjerknes forces are caused by a neighbouring bubbles or boundaries. The bubble becomes oblate along the bisector during collapsing, as the second Bjerknes forces are stronger for the parts of the bubble surfaces near the walls. The jet pointing towards the corner, due to the combined effects of the two second Bjerknes forces.

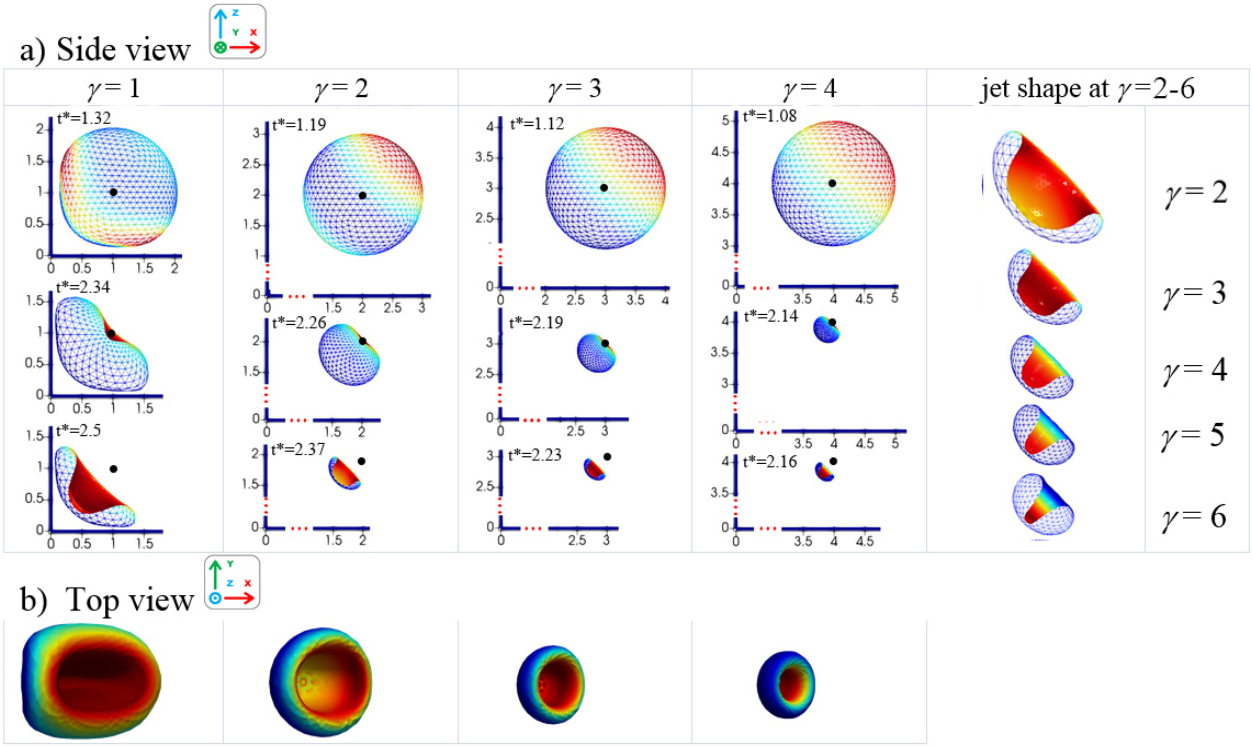

Figure 8. Bubble dynamics near a right-angled corner $\alpha = \pi/2$ at various standoff distances from the two walls $\gamma_N = \gamma_F = \gamma = 1, 2, 3, 4, 5, 6$: (a) Side view of the bubble shapes at inception (dot point), maximum volume, jet formation and jet impact, enlarged bubble shapes before jet impact, and (b) Top views of the enlarged bubble shape before impact. The remaining of parameters are set as $\beta = 0$, $R_m = 0.85$mm, $\varepsilon = 200$, $We = 1152$, $\delta = 0.009$ and $\kappa = 1.4$.

Figure 9 shows the bubble shapes in a smaller corner angle for $\alpha = \pi/4$. The bubble remains spherical during expansion except for $\gamma \leq 1$ for which it becomes elongated along the bisector direction. A jet forms towards the end of the collapse pointing to the corner (frame 3). The bubble

volumes at jet formation and jet impact and the jet width increase inversely with γ. These features are analogous to a bubble oscillating near a flat wall (Blake et al. 1986). Also, comparing figures 8 and 9, one can see that the bubble volumes at jet formation and jet impact and the jet width increase inversely with α. Note that the jet for $\gamma = 6$ is slightly asymmetric due to the numerical errors associated with the asymmetric mesh.

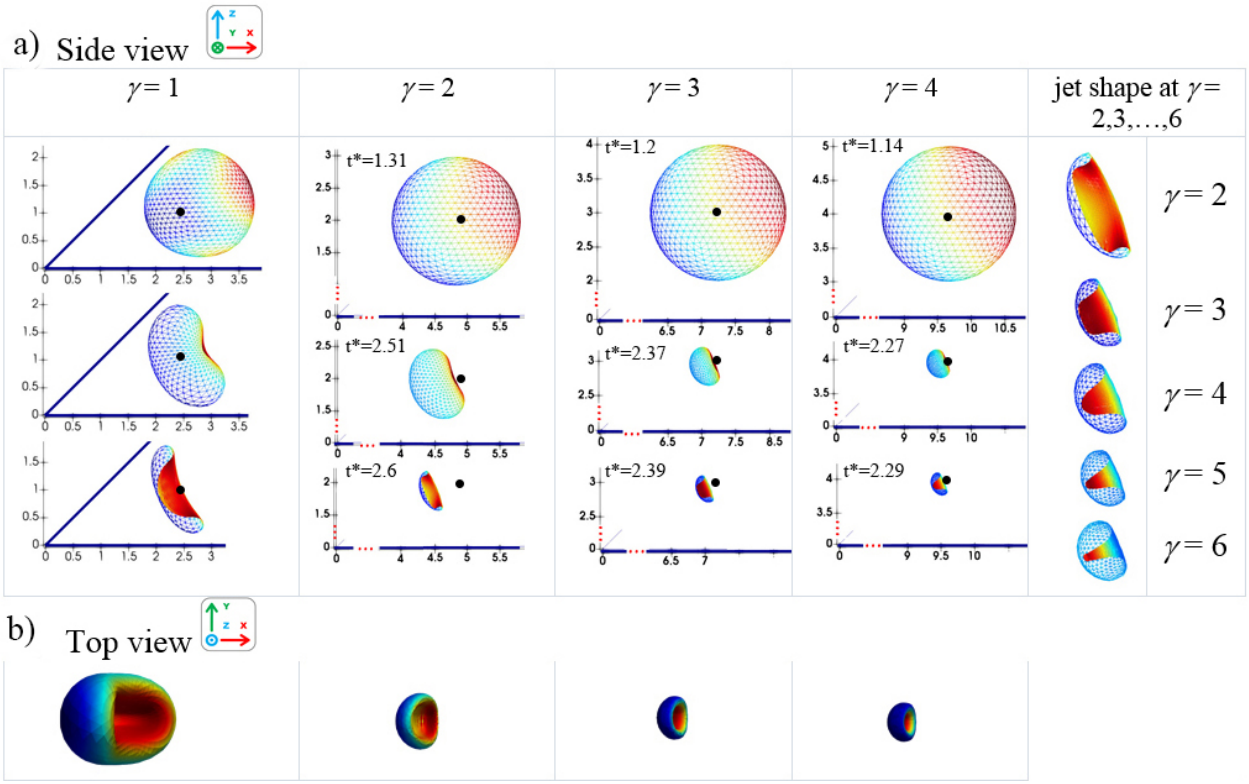

Figure 9. Bubble dynamics near a corner angled at $\alpha = \pi/4$ at various standoff distances from the two walls $\gamma_N = \gamma_F = \gamma = 1, 2, \ldots, 6$: (a) Side view of the bubble shapes at inception (dot point), maximum volume, jet formation and jet impact, enlarged bubble shapes before jet impact, and (b) Top views of the enlarged bubble shape before impact. The remaining parameters are the same as in figure 8.

Figure 10 shows the pressure contours and velocity fields in the flow domain for $\alpha = \pi/2$ and $\gamma = 1, 2$, with the remaining parameters being the same as figure 8. The pressure field loses spherical symmetry at the start of the expansion, even though the bubble is approximately spherical (frames a1, a2, b1 and b2). The pressure decreases radially and is relatively high near the corner (frames a1 and b1). The velocity decreases radially too and decreases faster on the wall sides. At the start of the collapse (frames a2 and b2), the pressure increases radially and is small in the corner and the flow becomes almost motionless there, stagnation points occurring on the bisector of the corner. The liquid far away from the bubble moves away and the liquid near the bubble surface opposite to the corner moves back, where the bubble first collapses. A stagnation point is formed on the bisector. During the later stages of the collapse, a high-pressure zone develops on the opposite side of the bubble to the corner (frames a3 and b3), which subsequently generates the jet and pushes the bubble towards the corner (frames a4 and b4). Similar features were observed for a bubble oscillating near a flat wall (Li et al. 2016). As the bubble is initiated closer to the corner, the pressure near the corner is larger during the early stages of the expansion and lower towards the end of the collapse.

The pressure near the corner is high at the beginning of expansion, where the liquid is compressed by the expanding bubble surface and confined by the corner. In contrast, the pressure near the corner is low during collapse, where the liquid is pulled by the receding bubble surface but constrained by the corner. During the collapse, the free inflow of liquid from the open side is faster, no longer pointing to the center of the bubble, but toward its top near the bisector of the corner. Thereby the pressure on the top of the bubble increases and the bubble gets indented by the liquid flow directed inwardly into the bubble toward the corner. Similar behaviour was noticed for a bubble collapsing near a flat rigid boundary by Blake et al. (1986).

Figure 11 displays the similar features of the pressure contours and velocity fields in the flow domain for $\alpha = \pi/4$, with other parameters being the same as in figure 10. However, a larger zone of higher pressure at the corner during the early stage of the expansion and a larger zone of lower pressure towards the end of the collapse are observed for $\alpha = \pi/4$. The high pressure zone near the base of the jet forms later, since the flow following the receding bubble surface along the walls are closer to the bisector than that for $\alpha = \pi/2$.

In this and some other cases, the bubble surface tends to keep in contact with walls once started. This did not cause any singularity problem in the computations as the normal velocity and normal derivative of the Green function are small in this region. Wang et al. (2015) discussed the following mechanism on this phenomenon. The pressure in the thin layer of liquid between the bubble and the boundary is approximately constant and equal to the pressure of the bubble gas. The flow velocity within the thin layer is close to zero. In addition, the surface tension effects tend to keep this part of the bubble surface, as the pressure is constant and equal at its two sides. Reuter & Kaiser (2019) measured the time evolution of the liquid-film thickness of a single cavitation bubble in water collapsing onto a solid surface. They found that during the first cycle of oscillation, the bubble does not come in direct contact with the solid surface.

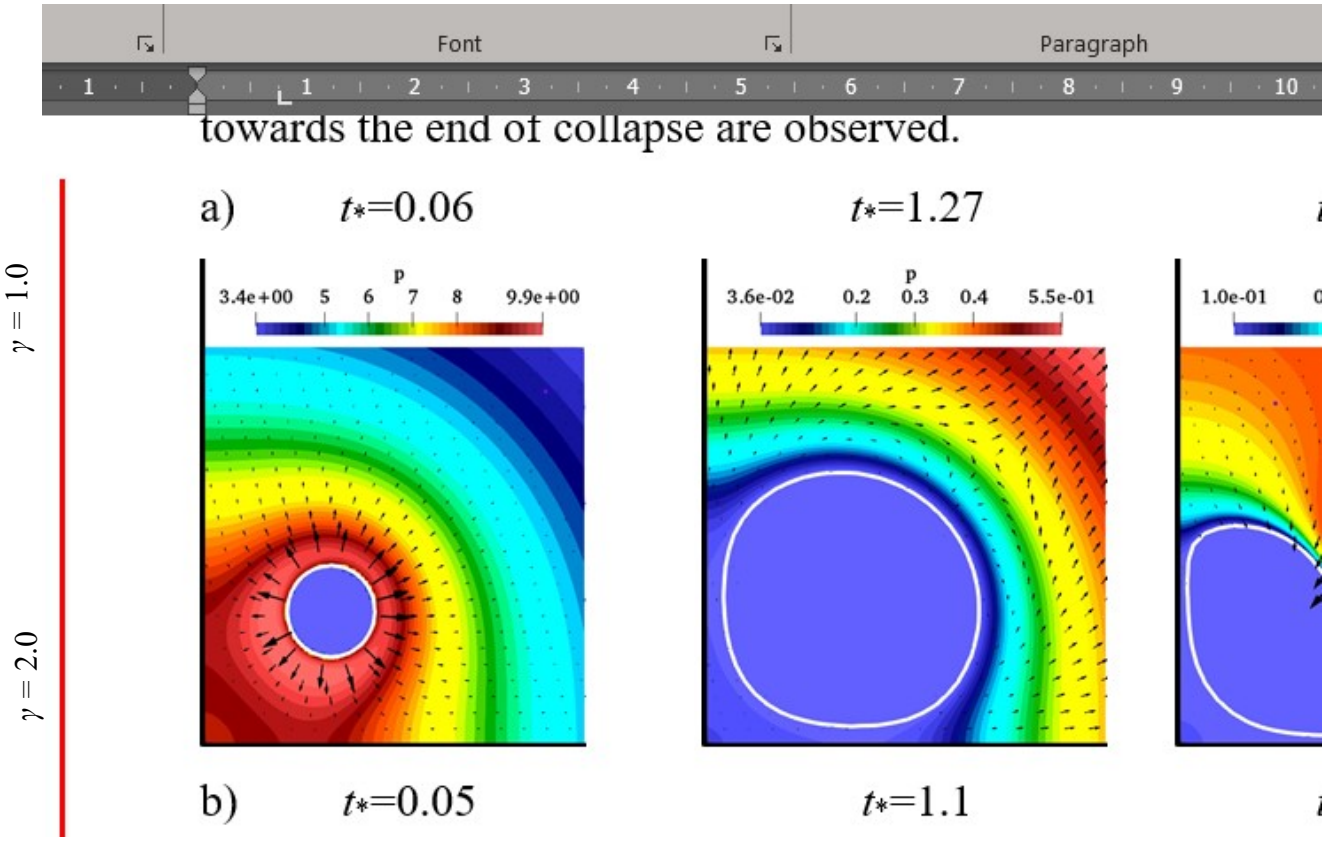

Figure 10. Pressure contours and velocity fields in the flow domain and normal velocity on the bubble surface for a bubble in a corner with $\alpha = \pi/2$ and at (a) $\gamma = 1.0$, (b) $\gamma = 2.0$, for the case shown in figure 8.

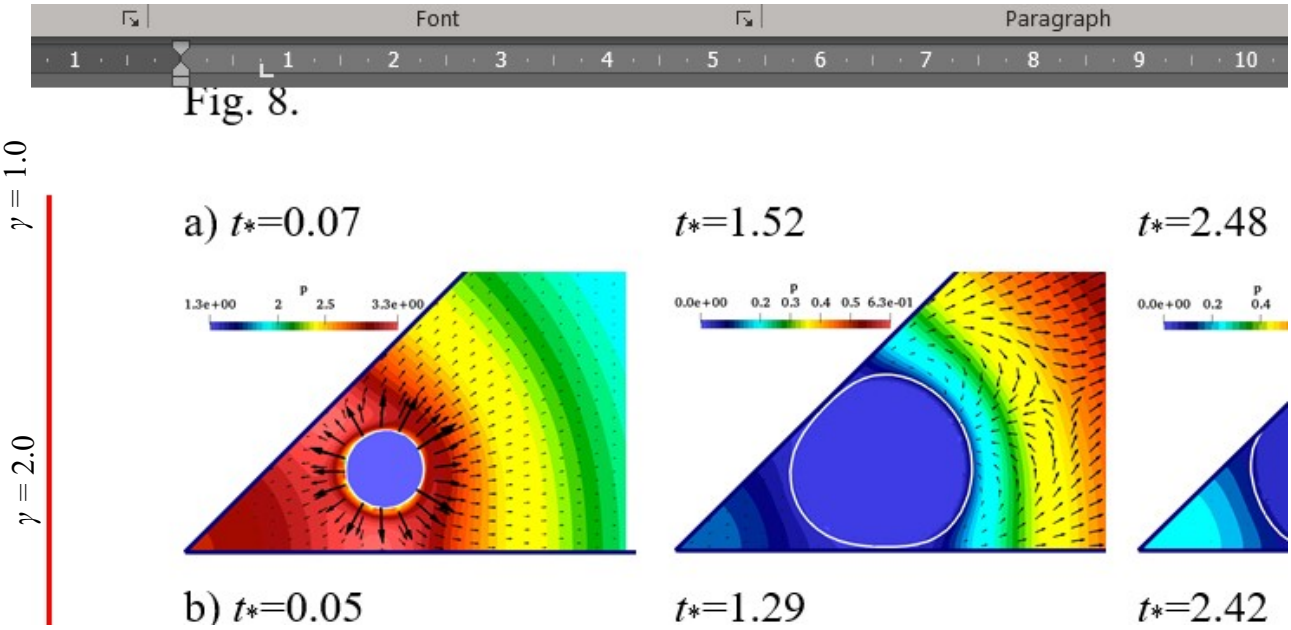

Figure 11. Pressure contours and velocity vectors for a bubble in a corner with $\alpha = \pi/4$, and at (a) $\gamma = 1.0$, and (b) $\gamma = 2.0$, for the case shown in figure 9.

Figures 12(a) and 12(b) show the time histories of the jet velocity v_{jet} and equivalent bubble radius R_{eq} for $\alpha = \pi/2$, and $\gamma = 1$, 2, 3, 4. As the bubble is initiated nearer the corner, the oscillation period increases and the jet velocity decreases. From $\gamma = 4$ to 1, the oscillation period increases by 12% and the dimensionless maximum jet velocity decreases from 17.8 to 3.5. Figures 12(c) and 12(d) show the time histories for $\alpha = \pi/2$, $\pi/4$, $\gamma = 1$, 4. For comparison, we also display the results for a bubble near a rigid flat boundary ($\alpha = \pi$). For a smaller corner angle, the oscillation period increases and the jet velocity decreases. For $\gamma = 1$, the oscillation period increases by 10% and the maximum jet velocity decreases by 21% as α is decreases from $\pi/2$ to $\pi/4$.

oscillation period increases and the jet velocity decr

increases by 10% and the maximum jet velocity decre

π/4.

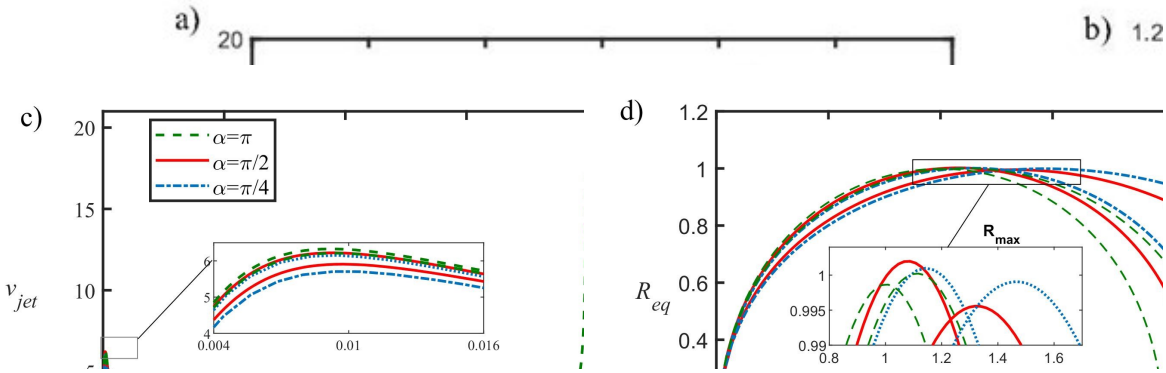

Figure 12. Time histories of (a, c) the jet velocity v_{jet} and (b, d) the equivalent bubble radius R_{eq} for the cases shown in figures 8 and 9, respectively.

For a bubble nearer to rigid boundaries, both its expansion and collapse are slowed down by the blocking of the boundaries. Their oscillation periods thus decrease. This differs from a bubble in a fully confined domain, where the volume within the confinement is fixed for a rigid confinement or with limited change for an elastic confinement. While the bubble oscillates, the liquid is compressed or expanded, therefore the compressible effects of a liquid enhances the stiffness of the oscillation system (Wang 2017, Liu et al. 2018). Consequently the natural frequency of oscillation for a bubble in a confinement is larger, in order of magnitude, than that in an unbounded liquid.

For a larger value of γ less than about 5, the higher jet speed occurs because the bubble has the opportunity to collapse to a smaller size, and hence higher velocities and pressures. This is true for bubbles near a rigid boundary (Blake et al. 1986). As γ is about larger than 5, the asymmetric effects are weak and bubble minimum volume does not change significantly with γ, the jet velocity decreases with γ. Lechner et al. (2019) observed a different type of axial jet with very high speed for a bubble being in extreme vicinity to a solid boundary for $\gamma \lessapprox 0.2$, which is formed by an annular-liquid-flow collision.

Figure 13 displays the time history of the displacement of the bubble centroid $d_c(t)$ for cases shown in figures 8 and 9. For the case of a bubble near a rigid flat boundary, $d_c(t)$ is the distance from the bubble centroid to the boundary. The bubble moves away from the corner during expansion along the bisector and moves back at much higher amplitude during the collapse. The migration amplitude decreases with γ and increases with α. These trends have been verified in our calculations for $1 \leq \gamma \leq 20$.

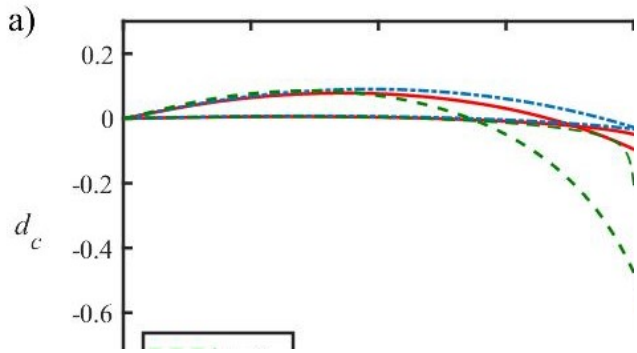

Figure 13. Time history of the displacement of the bubble centroid, for the cases in figures 8 and 9.

Figure 14 displays the jet velocity and displacement amplitude of the bubble centroid $d_c(t)$ before jet impacting on the opposite bubble wall. The jet velocity firstly increases with the standoff distance γ from the corner, reaches the maximum around $\gamma = 5$ and after that decreases. The displacement amplitude $d_c(t)$ firstly increases and then decreases with γ too, but reaching the maximum much earlier around $\gamma = 1.5$. Both the jet velocity and displacement amplitude increases with the corner angle α.

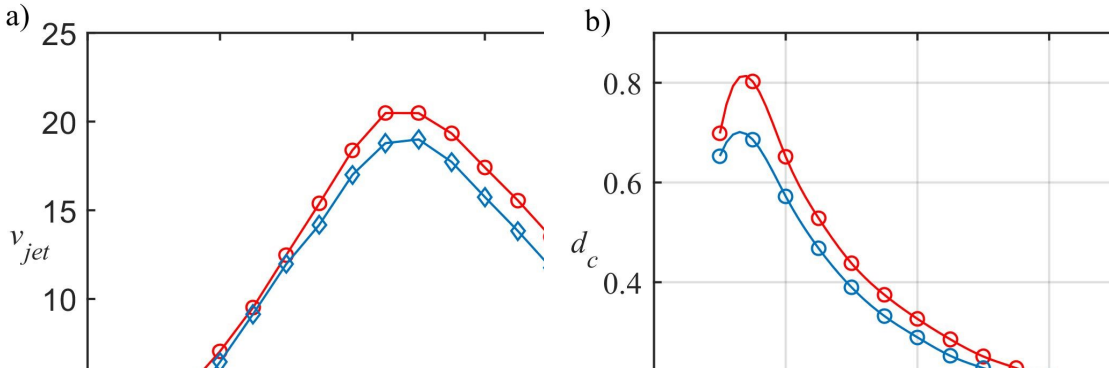

Figure 14. Comparison of the (a) jet velocity, and (b) bubble centroid displacement versus γ for $\alpha = \pi/2$ (red-line) , and $\alpha = \pi/4$ (blue-line), for the cases in figures 8 and 9.

5.2 *The asymmetric case* ($\beta \neq 0$)

Figure 15 shows the bubble shapes for the asymmetric cases ($\beta \neq 0$), for $\alpha = \pi/2$, $\gamma_N = 1$ and $\gamma_F = 2$, 3, 6 and 15. Each row in figure 15(a) illustrates the bubble shapes at the inception, maximum bubble volume, jet formation and immediately before the jet impact. The bubble expands spherically for all of the cases, except for the near bubble surface which is flattened by the near wall. The bubble is symmetric to the vertical plane to the near wall passing through its geometrical centre for $\gamma_F \geq 2$. During the later stages of the collapse (the third row), the bubble develops a non-spherical, asymmetry for $\gamma_F \leq 3$ but approximately symmetric to the plane vertical to the near wall for $\gamma_F \geq 6.5$. The jet starts to form on the part of the bubble surface opposite to the near wall and further away from the far wall. Towards the end of the collapse, the jet is approximately pointing to the near wall, but inclined to the further wall as γ_F decreases. The bubble volumes at jet formation and jet impact and the jet width decrease with γ_F.

Figure 16(a) shows the corresponding bubble shapes for $\alpha = \pi/4$. The jet is approximately pointing vertically to the near wall for $\gamma_F = 15$ but inclined to the further wall as γ_F decreases. Here, the jet is more inclined to the further wall, and it is wider compared with the case for $\alpha = \pi/2$.

Figures 15(b) and 16(b) show the top view, (x-y plane), of the bubble shape immediately before the jet impact. It is observed that the bubble is elongated along the symmetrical plane of the configuration. This effect reduces with increasing γ_F and the top view of the bubble and jet shapes become axisymmetric for $\gamma_F \geq 6.0$.

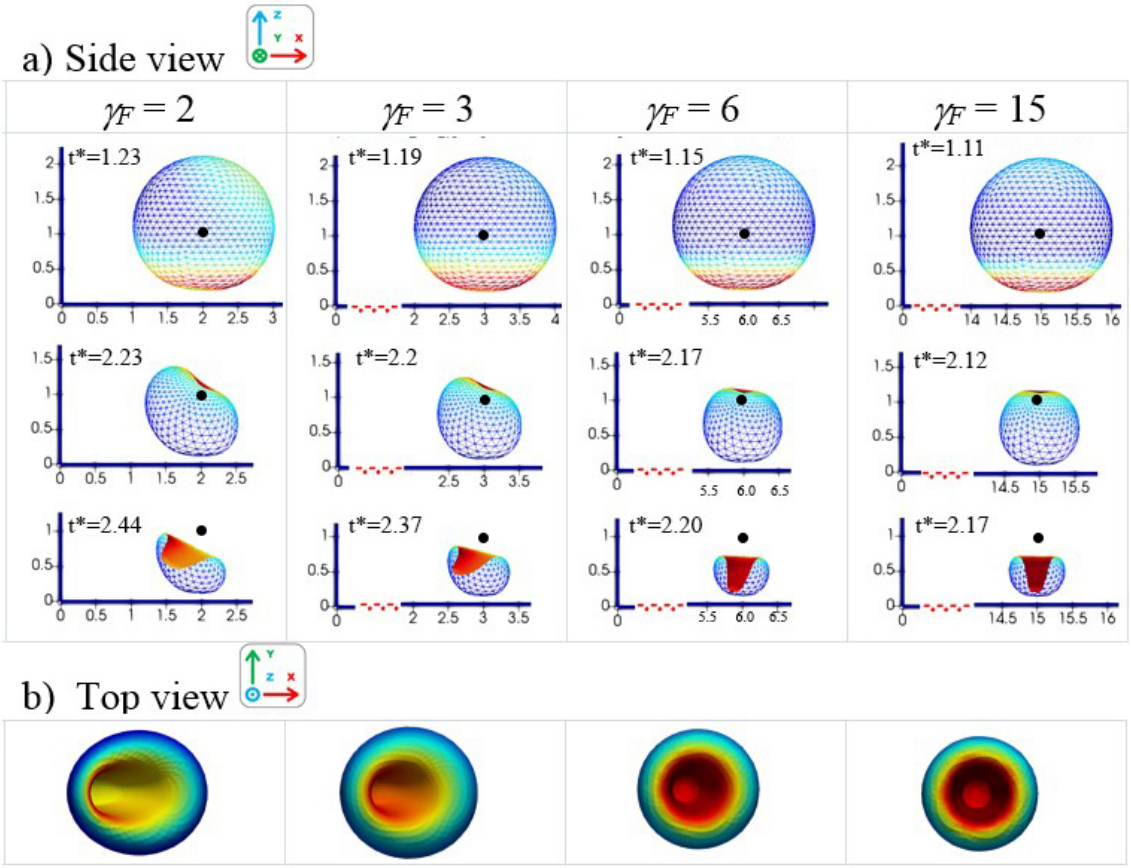

Figure 15. Bubble shapes at different views for $\gamma_N = 1$, various values of γ_F, and $\alpha = \pi/2$, (a) *xz*-coordinate view, and (b) *xy*-coordinate view. The remaining parameters are the same as in figure 8.

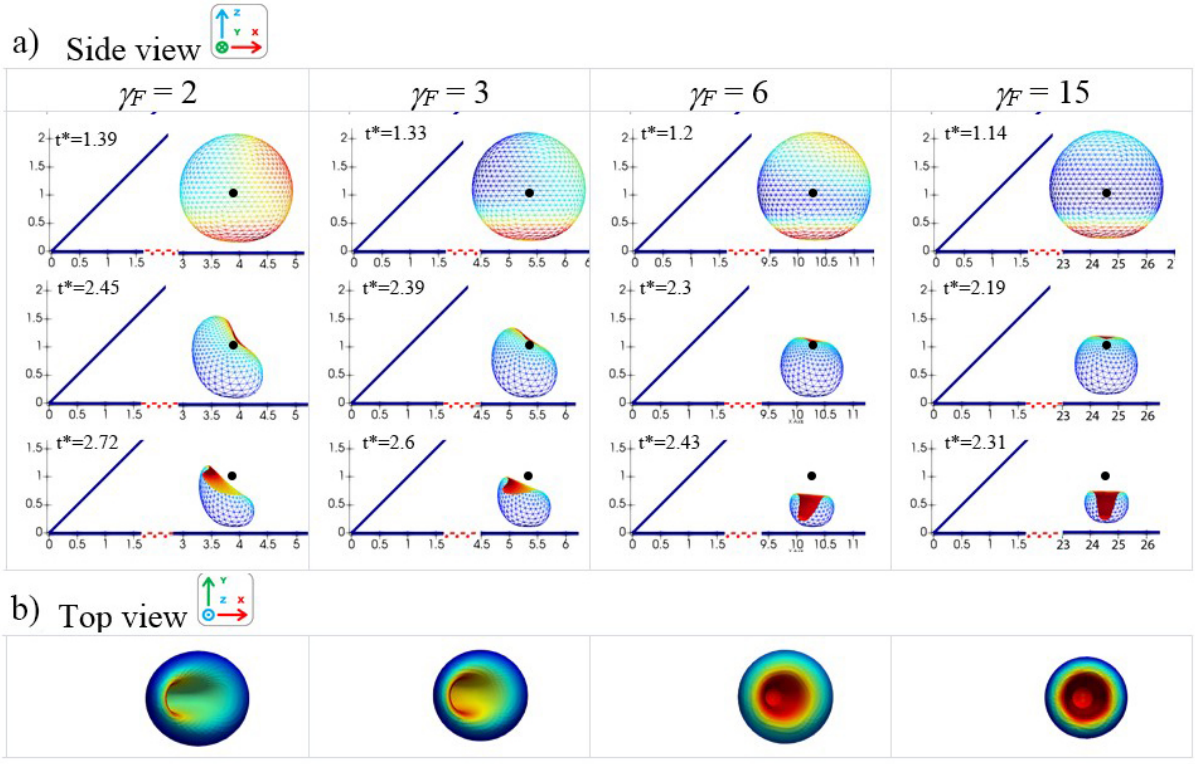

Figure 16. Bubble shapes at different views for $\gamma_N = 1$, various values of γ_F, and $\alpha = \pi/4$, (a) *xz*-coordinate view, and (b) *xy*-coordinate view. The remaining parameters are the same as in Figure 8.

Figure 17 presents the pressure contours and velocity vectors for a bubble in a corner with $\alpha = \pi/2$, $\gamma_N = 1$, $\gamma_F = 2.0$ in figure 17(a), $\gamma_F = 3.0$ in figure 17(b) and the remaining parameters are the same as in figure 8. During the early stages of the expansion, the pressure decreases radially from the bubble and is relatively high between the bubble and the near wall (frames a1 and b1). The velocity decreases radially too but decreases faster on the wall sides. At the start of the collapse, the pressure increases further away and is relatively low between the bubble and the near wall (frames a2 and b2). The liquid in the far field flows outwards and the liquid near the part of the surface opposite to the near wall and further away from the far wall recedes, where the bubble first collapses, resulting in a stagnation point between the bubble and the far field. In the late stages of collapse (frames a3 and b3), a high-pressure zone develops above the bubble and away from the far wall, which subsequently generates the jet towards the near wall, but inclined to the far wall (frames a4 and b4). During the period of jet development, the high-pressure zone moves towards the far wall. As the bubble is initiated nearer to the corner, the pressure field displays stronger asymmetry in the vertical plane to the near wall passing through the bubble centroid, and the high-pressure zone is more inclined away from the vertical plane.

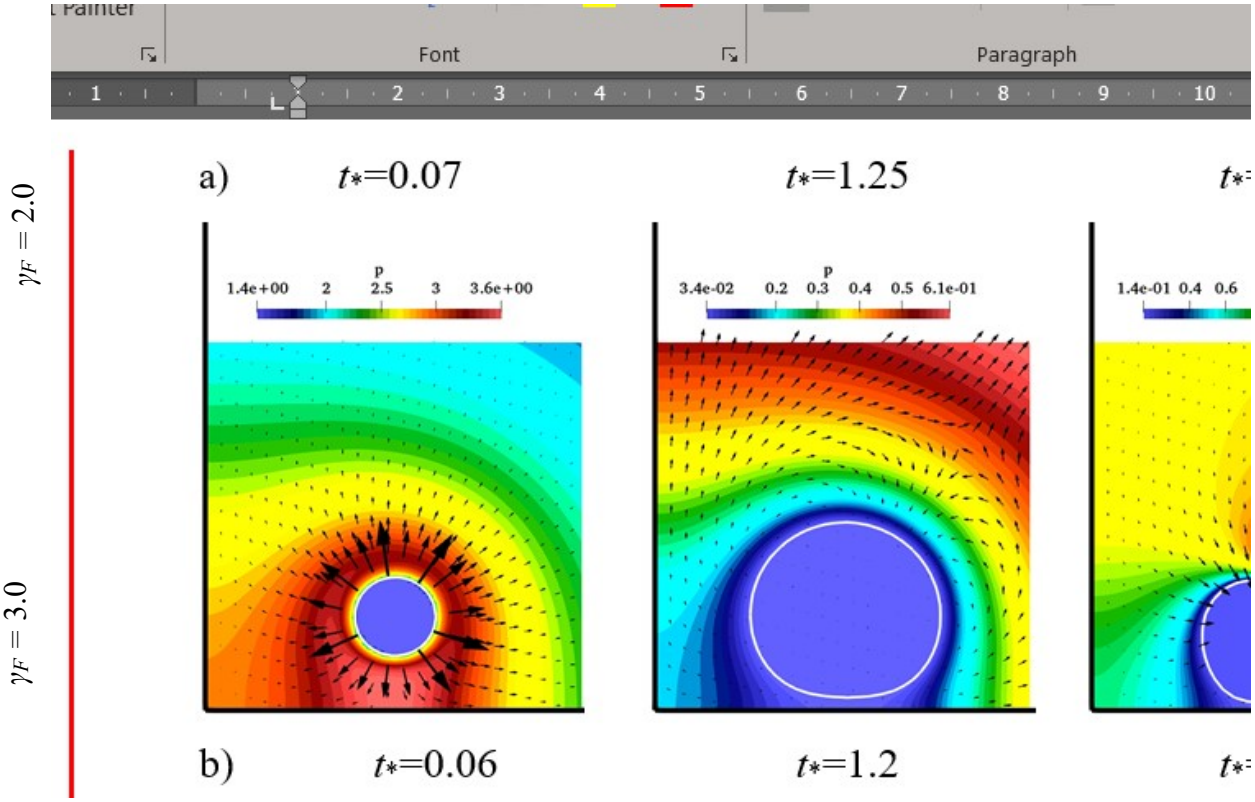

Figure 17. Pressure contours and velocity vectors for a bubble in a corner for $\alpha = \pi/2$, $\gamma_N = 1$, and (a) $\gamma_F = 2.0$, (b) $\gamma_F = 3.0$, for the cases in figure 15.

Figure 18 displays similar features of the pressure contours and velocity vectors in the domain for a bubble in a corner with $\alpha = \pi/4$, $\gamma_N = 1$, $\gamma_F = 2.0$ in figure 18(a), $\gamma_F = 3.0$ in figure 18(b) and the remaining parameters are the same as in figure 8. During the early stages of the expansion (collapse), the pressure decreases (increases) radially, quickly in the open side but slowly towards the near-wall. A velocity stagnation point forms at the start of the collapse and high-pressure zone

forms during the late stages of the collapse above the bubble and away from the far wall. The asymmetry of the pressure field to the plane vertical to the near-wall passing through the bubble centre is stronger than that for $\alpha = \pi/2$.

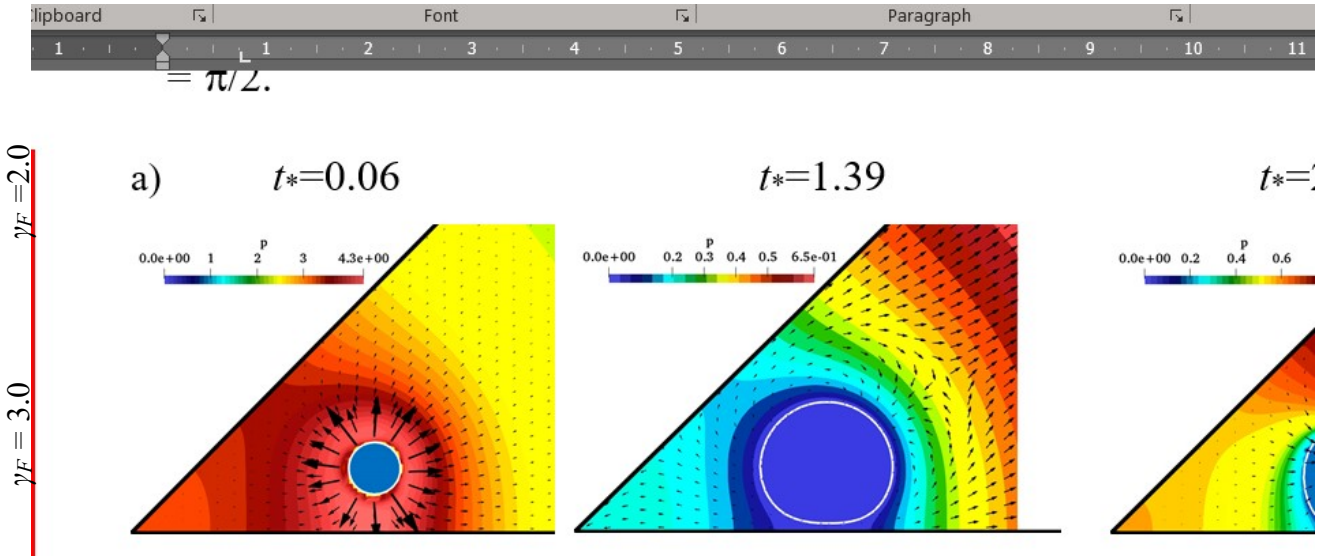

Figure 18. Pressure contours and velocity vectors for a bubble in a corner with $\gamma_N = 1$ and $\alpha = \pi/4$, (a) $\gamma_F = 2.0$, (b) $\gamma_F = 3.0$, for the cases in figure 15.

Figures 19(a) and 19(b) show the time histories of the jet velocity v_{jet} and the equivalent bubble radius R_{eq}, respectively, for $\alpha = \pi/2$, $\gamma_N = 1$ and $\gamma_F = 1, 2, 3, 4$. The period of bubble oscillation decreases with γ_F but the jet velocity increases with γ_F. Figures 19c and 19d show the time histories of jet velocity v_{jet}, and the equivalent bubble radius R_{eq} and for $\alpha = \pi/2, \pi/4$ and $\gamma_F = 1, 4$. The period decreases with α but the jet velocity increases with α. The maximum bubble volume does not change significantly with α and γ_F.

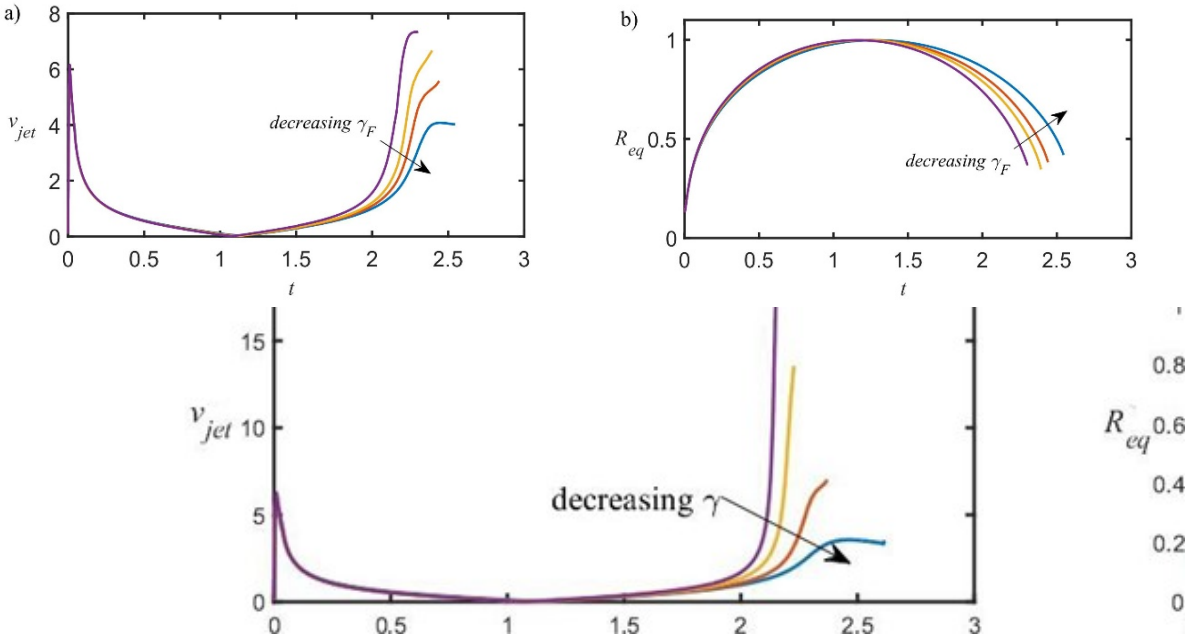

Figure 19. Time histories of (a) the jet velocity v_{jet}, and (b) the equivalent bubble radius R_{eq} for $\alpha = \pi/2$, $\gamma_N = 1$ and $\gamma_F = 1, 2, 3, 4$; (c) jet velocity v_{jet}, and (d) the equivalent bubble radius R_{eq} for $\alpha = \pi/2, \pi/4$, $\gamma_N = 1$ and $\gamma_F = 1, 4$, for the cases in figures 15 and 16.

Figures 20(a) and 20(b) show the displacements of the bubble centred (x_c, z_c) versus time. The bubble migrates away from the near wall and corner during expansion and moves back to the near wall and corner during collapse at much larger speed and amplitude. This is analogous to a bubble oscillating near a wall, migrating away from the wall during expansion and moves back during collapse (Blake et al. 1986). The amplitude of migration towards the corner, x_c, decreases with γ_F but increases with α. The amplitude of migration perpendicular to the near wall, z_c, increases both with γ_F and α. These trends are consistent to the time histories of the Kelvin impulse shown in figure 21. The x-component of the Kelvin impulse decreases with γ_F but increases with α, whereas the y-component of the Kelvin impulse increases with both γ_F and α.

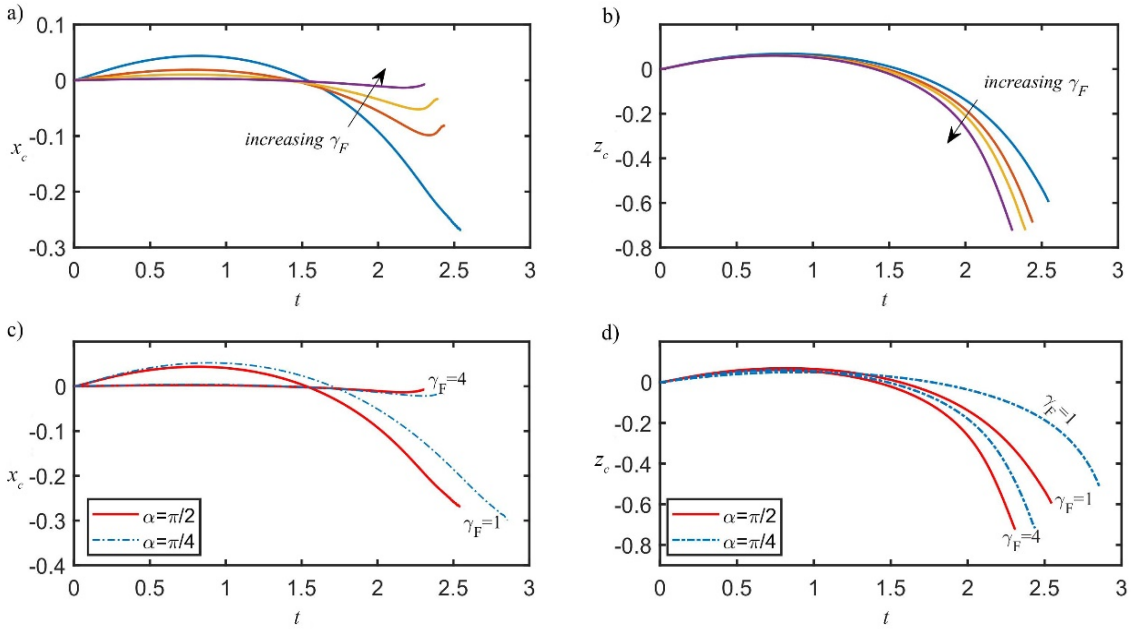

Figure 20. Displacements of the centroid for a bubble in a corner: (a) parallel to the near wall, x_c, (b) perpendicular to the near wall, z_c, for $\alpha = \pi/2$, $\gamma_N = 1$ and $\gamma_F = 1, 2, 3, 4$; (c) parallel to the near wall, x_c, (d) perpendicular to the near wall, z_c, for $\gamma_N = 1$ and $\gamma_F = 1, 4$, $\alpha = \pi/2$, $\alpha = \pi/4$, for the cases in figures 15 and 16.

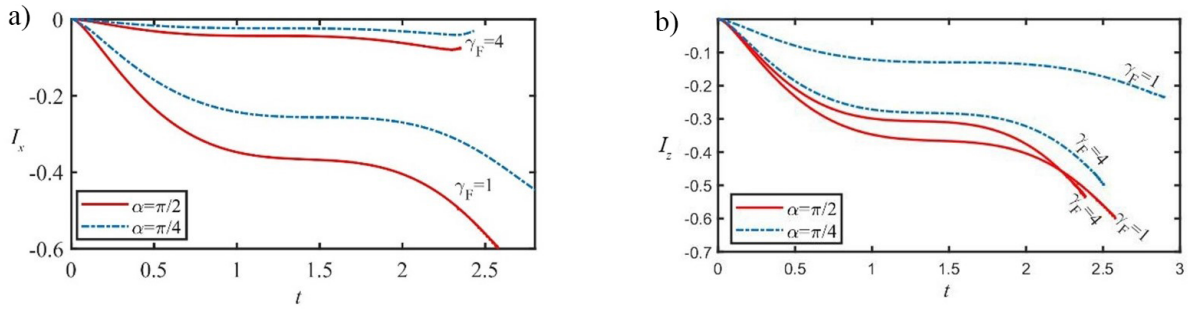

Figure 21. Time histories of the Kelvin impulse (a) I_x and (b) I_z for $\alpha = \pi/2$ (b) for $\alpha = \pi/4, \pi/2$, and γ_F=1, 4 for the cases in figures 15 and 16.

Figure 22 compares the directions of the Kelvin impulse and the jet direction. The directions of the Kelvin impulse are obtained using both the analytical result (18), θ_F, and the BIM result, θ_I. The jet is not symmetric as $\beta \neq 0$, so its direction θ_{jet} is defined in terms of its basement direction as shown in figure 22(a). The jet angle θ_{jet} to the near wall increases with γ_F and approaches π/2 as $\gamma_F \geq 10$. The directions of the Kelvin impulse and the jet have excellent agreement.

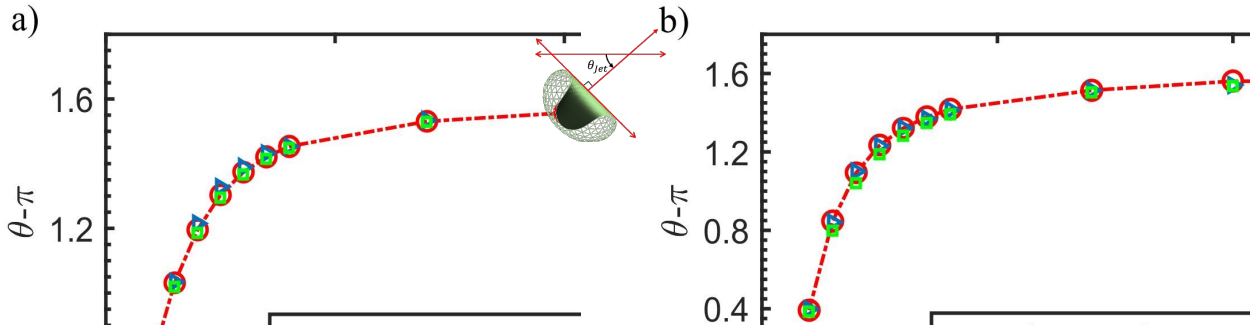

Figure 22. Comparison of the directions of the Kelvin impulse θ_F and θ_I, the displacement of the geometrical centre just before the jet impact θ_{jet}, (a) $\alpha = \pi/2$ and (b) $\alpha = \pi/4$, for $\gamma_N = 1$ and $\gamma_F \in [1, 15]$. The remaining parameters are the same as figure 8.

6. The dynamics of microbubble in a corner

In this section, we consider the simulation for microbubbles having the maximum bubble radius R_m = 5, 10, 15 , 20 and 25μm with the corresponding Reynold number Re = 49, 99, 149, 199 and 249 respectively. R_m denotes the maximum bubble radius that the bubble achieves in an infinite domain without viscous and surface tension effects. The bubble evolution and jet shapes are displayed in figure 23 and the time histories of the jet velocity, bubble equivalent radius, centroid motion and Kelvin impulse are shown in figure 24.

For smaller bubbles, the maximum bubble radius acheived and oscillation period decrease, because its energy is lost due to viscous effects and owned by surface tension. The energy of a bubble system is lost due to the viscous effects and the acoustic radiation associated with the emission of shockwaves. Shockwaves emitted at the minimum bubble volumes after bubble jets penetrate bubbles (Wang 2016), which are not considered in this paper. As the maximum bubble radius decreases, the effectively dimensionless standoff distance from the walls increases and the associated wall effects decreases too. This results in stronger collapse, smaller bubble volume before jet impact, higher jet velocity, less migration of the bubble centroid to the walls and weaker Kelvin impulse.

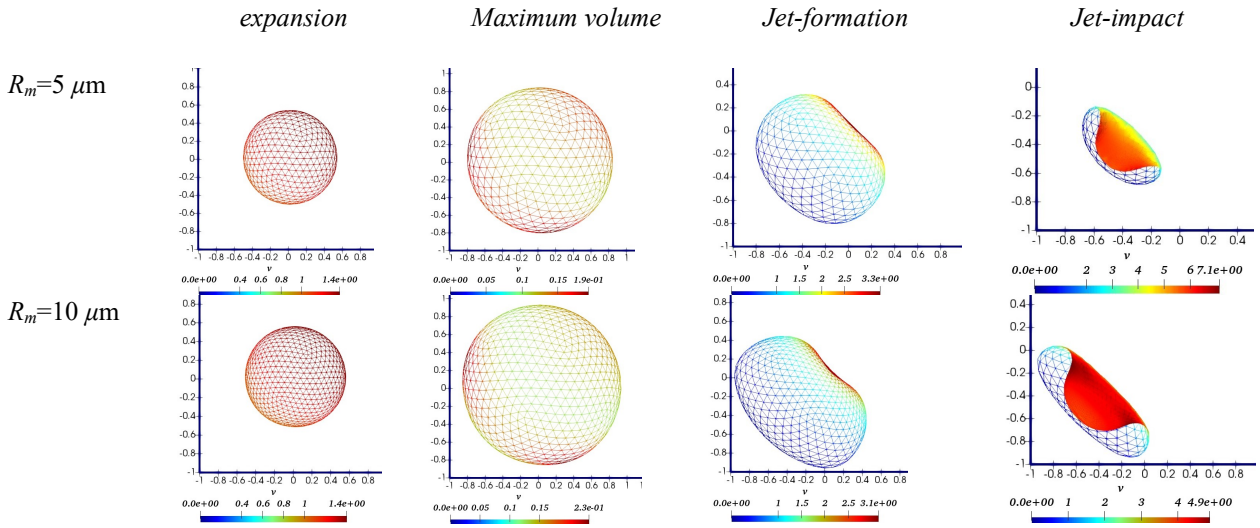

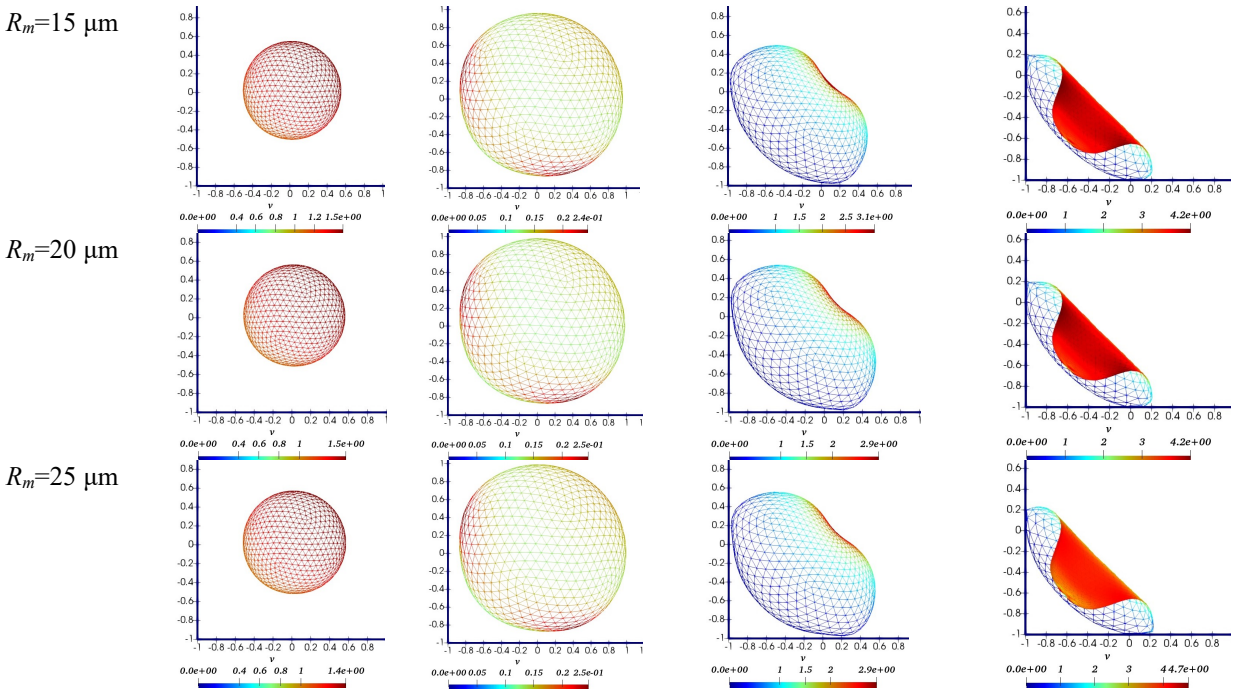

Figure 23. Bubble dynamics near a right-angled corner $\alpha = \pi/2$ for various bubble size at R_m = 5, 10, 15, 20 and 25 μm with the corresponding Reynolds's numbers Re = 49, 99, 149, 199 and 249, and Weber numbers We=6.8, 13.5, 20.3, 27.1 and 33.8, respectively. The remaining parameters are set as $\gamma = 1$, $\beta = 0$, $\varepsilon = 200$ and $\kappa = 1.4$.

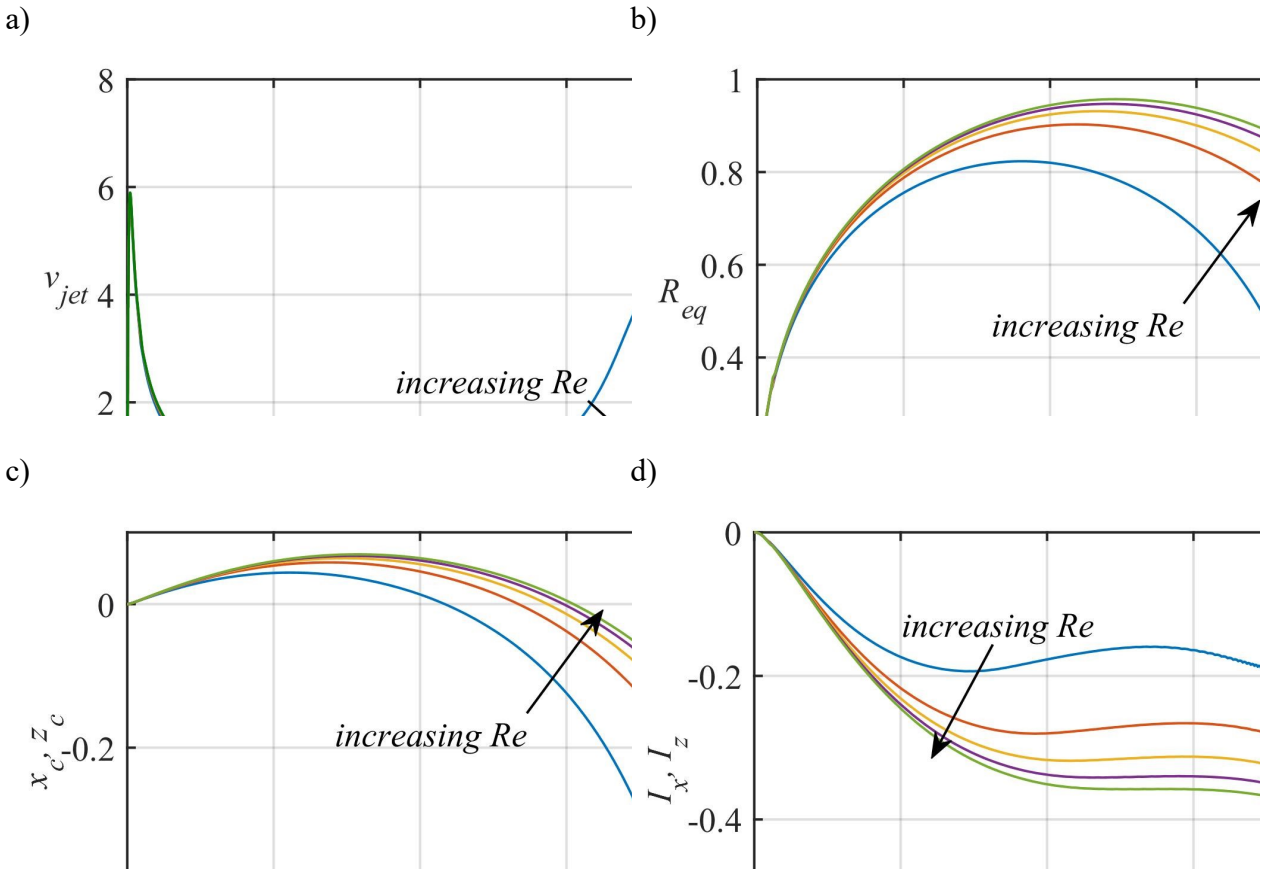

Figure 24. Time histories of (a) the jet velocity v_{jet}, (b) the equivalent bubble radius R_{eq}, (c) displacements of the bubble centroid x_c, z_c, and (d) Kelvin impulse I, for the cases shown in figure 23.

7. Conclusions

In this paper, we have considered the growth and collapse of a bubble in a corner subject to the secondary Bjerknes forces due to the walls. The bubble expands approximately spherically, except for the bubble surfaces near walls which are compressed by the walls. Physically the sides of the bubble nearer the walls will move into a region of higher relative impedance than other sides. During the latter stages of the collapse, the bubble initiated at the bisector of the corner becomes oblate along the bisector, as the secondary Bjerknes forces are stronger for the parts of the bubble surfaces near the walls. A high-speed liquid jet then forms pointing towards the corner, due to the combined effects of the two secondary Bjerknes forces. For a bubble initiated away from the bisector, the jet is approximately pointing to the near wall but inclined to the corner, when the Bjerknes force due to the near wall is dominant.

The pressure field loses spherical symmetry during the early stages of the expansion long before the bubble becomes non-spherical. A velocity stagnation point forms at the start of the collapse and a high pressure zone forms during the latter stages of the collapse at the base of the jet, which subsequently drives the jet. As the bubble is initiated near the corner, the pressure field displays strong asymmetry to the vertical plane to the near wall passing through the bubble centroid. The asymmetry is stronger for a smaller corner angle.

For a smaller standoff distance to the corner or for a smaller corner angle, the oscillation period, the bubble volumes at the start of the jet formation and jet impact, and the width of the jet increase, whereas the jet velocity decreases.

The bubble migrates away from the near wall and corner during its expansion and moves back to the near wall and corner during its collapse, but at much larger speed and amplitude. The amplitude of migration towards the corner decreases with the standoff distance to the corner but increases with corner angle. The amplitude of migration perpendicular to the near wall increases with both of them, as the second Bjerknes force due to the far wall decreases. These trends are consistent with the time histories of the Kelvin impulse. The Kelvin impulse theory is shown to predict the jet direction accurately.

The bubble migration and jetting towards the near wall and the corner show that there are no blind spots in the cavitation cleaning of a corner in terms of the jetting, the acoustic microstreaming and the associated shear stress. However, the combined effect of the decrease in jet velocity and the increase of jet width for smaller corner angles is worthy of further investigation for the cleaning of the vertex in these corners.

Acknowledgements

This work was supported by the Engineering and Physical Sciences Research Council (EPSRC) through Grant No. EP/P015743/1.

REFERENCES

Abramowitz, M. and Stegun, I.A., 1965. *Handbook of mathematical functions: with formulas, graphs, and mathematical tables* (Vol. 55). Courier Corporation

Blake, J. R. & Gibson, D. C. (1987), 'Cavitation bubbles near boundaries', *Annu. Rev. Fluid Mech*. **19**(1), 99–123.

Blake, J. R., Leppinen, D. M. & Wang, Q. X. (2015), 'Cavitation and bubble dynamics: the Kelvin impulse and its applications', *Interface focus* **5**(5), 20150017.

Blake, J. R., Taib, B. B. & Doherty, G. (1986), 'Transient cavities near boundaries. Part 1. Rigid boundary', *J. Fluid Mech*. **170**, 479–497.

Brennen, C. E. 2013 Cavitation and Bubble Dynamics, Oxford University Press (available online).

Brennen, C.E. (2015) Cavitation in medicine. Interface Focus 5, 20150022.

Brujan, E. A., Keen, G. S., Vogel, A. & Blake, J. R. (2002), 'The final stage of the collapse of a cavitation bubble close to a rigid boundary', *Phys. Fluids* **14**(1), 85–92.

Brujan, E.-A. & Matsumoto, Y. (2012), 'Collapse of micrometer-sized cavitation bubbles near a rigid boundary', *Microfluid Nanofluid*. **13**(6), 957–966.

Brujan, E.-A., Noda, T., Ishigami, A., Ogasawara, T. & Takahira, H. (2018), 'Dynamics of laser-induced cavitation bubbles near two perpendicular rigid walls', *J. Fluid Mech*. **841**, 28–49.

Chahine, G. L., Kapahi, A., Choi, J.-K. & Hsiao, C.-T. (2016), 'Modeling of surface cleaning by cavitation bubble dynamics and collapse', *Ultrason. Sonochem*. **29**, 528–549.

Coussios, C. C. and Roy, R. A. 2007 Applications of Acoustics and Cavitation to Non-invasive Therapy and Drug Delivery. Annu. Rev. Fluid Mech. 40, 395-420.

Curtiss, G. A., Leppinen, D. M., Wang, Q. X. & Blake, J. R. (2013), 'Ultrasonic cavitation near a tissue layer', *J. Fluid Mech*. **730**, 245–272.

Hsiao, C.-T., Jayaprakash, A., Kapahi, A., Choi, J.-K. & Chahine, G. L. (2014), 'Modelling of material pitting from cavitation bubble collapse', *J. Fluid Mech*. **755**, 142–175.

Joseph, D. D. & Wang, J. (2004) The dissipation approximation and viscous potential flow. J. Fluid Mech., 505, 365-377.

Joseph, D.D., Funada, T. & Wang, J. (2007) Potential flows of viscous and viscoelastic fluids. Cambridge University Press.

Kim, W. Kim, T. H., Choi, J. and Kim, H. Y. (2009) Mechanism of particle removal by megasonic waves. Applied Physics Letters 94, 081908.

Koukouvinis, P., Gavaises, M., Supponen, O. and Farhat, M. (2016) Numerical simulation of a collapsing bubble subject to gravity. Phys. Fluids 28, 032110.

Kucera, A. & Blake, J. R. (1990), 'Approximate methods for modelling cavitation bubbles near boundaries', *B. Aust. Math Soc*. 41(1), 1–44.

Lauterborn, W. & Bolle, H. (1975), 'Experimental investigations of cavitation-bubble collapse in the neighbourhood of a solid boundary', *J. Fluid Mech*. **72**(2), 391–399.

Lauterborn, W. & Kurz, T. (2010), 'Physics of bubble oscillations', *Rep. Prog. Phys*. **73**(10), 106501.

Lechner, C., Koch, M., Lauterborn, W. & Mettin, R. (2017), 'Pressure and tension waves from bubble collapse near a solid boundary: A numerical approach', *J. Acoust. Soc. Am*. **142**(6), 3649–3659.

Lechner, C., Lauterborn, W., Koch, M. & Mettin, R. (2019) Fast, thin jets from bubbles expanding and collapsing in extreme vicinity to a solid boundary: A numerical study. Phys. Rev. Fluids 4, 021601(R).

Li, S., Han, R., Zhang, A. M. & Wang, Q. X. (2016), 'Analysis of pressure field generated by a collapsing bubble', *Ocean Eng*. **117**, 22–38.

Lindau, O. & Lauterborn, W. (2003), 'Cinematographic observation of the collapse and rebound of a laser-produced cavitation bubble near a wall', *J. Fluid Mech*. **479**, 327–348.

Liu, Y. L., Wang, Q. X., Wang, S. P. & Zhang, A. M. (2016), 'The motion of a 3D toroidal bubble and its interaction with a free surface near an inclined wall', *Phys. Fluids* **28**(12), 122101.

Liu, Y.Q., Wang, Q.X. & Zhang, A.M. (2018) Surface stability of a bubble in a liquid fully confined in an elastic solid. Phys. Fluids 30, 127106.

Manmi, K. and Wang, Q. X. 2017 Acoustic microbubble dynamics with viscous effects. Ultrasonics Sonochemistry, 36, 427-436.

Ohl, S. P. & Allison, R. E. (2006), Ultrasonic inline inspection of the Moomba to Sydney pipeline, *in* 'Proceedings of the 6th International Pipeline Conference, Calgary, AB, Canada', pp. 25–29.

Philipp, A. & Lauterborn, W. (1998), 'Cavitation erosion by single laser-produced bubbles', *J. Fluid Mech*. **361**, 75–116.

Reuter, F. and Kaiser, S.A. (2019) High-speed film-thickness measurements between a collapsing cavitation bubble and a solid surface with total internal reflection shadowmetry. Phys. Fluids 31, 097108.

Rosselló, J. M., Lauterborn, W., Koch, M., Wilken, T., Kurz, T.and R. Mettin (2018) Acoustically induced bubble jets. Phys. Fluids 30, 122004.

Supponen, O., Obreschkow, D., Kobel, P., Tinguely, M., Dorsaz, N. & Farhat, M. (2017), 'Shock waves from nonspherical cavitation bubbles', *Phys. Rev. Fluid* **2**(9), 093601.

Supponen, O., Obreschkow, D., Tinguely, M., Kobel, P., Dorsaz, N. & Farhat, M. (2016), 'Scaling laws for jets of single cavitation bubbles', *J. Fluid Mech*. **802**, 263–293.

Szeri, A. J., Storey, B. D., Pearson, A. & Blake, J. R. (2003), 'Heat and mass transfer during the violent collapse of nonspherical bubbles', *Phys. Fluids* **15**(9), 2576–2586.

Tagawa, Y. & Peters, I. R. (2018), 'Bubble collapse and jet formation in corner geometries', *Phys. Rev. Fluid* **3**(8), 081601.

Tanizawa, K. (1995), A nonlinear simulation method of 3-d body motions in waves: formulation with the acceleration potential, *in* '10th Workshop on Water Waves and Floating Bodies, Oxford'.

Tomita, Y., Robinson, P. B., Tong, R. P. & Blake, J. R. (2002), 'Growth and collapse of cavitation bubbles near a curved rigid boundary', *J. Fluid Mech*. **466**, 259–283.

Tomita, Y. & Shima, A. (1986), 'Mechanisms of impulsive pressure generation and damage pit formation by bubble collapse', *J. Fluid Mech*.**169**, 535–564.

Vogel, A., Lauterborn, W. & Timm, R. (1989), 'Optical and acoustic investigations of the dynamics of laser-produced cavitation bubbles near a solid boundary', *J. Fluid Mech*. **206**, 299–338.

Vyas, N., Dehghani, H., Sammons, R., Wang, Q., Leppinen, D. & Walmsley, A. (2017), 'Imaging and analysis of individual cavitation microbubbles around dental ultrasonic scalers', *Ultrasonics* **81**, 66–72.

Vyas, N., Pecheva, E., Dehghani, H., Sammons, R. L., Wang, Q. X., Leppinen, D. M. & Walmsley, A. D. (2016), 'High speed imaging of cavitation around dental ultrasonic scaler tips', *PloS One* **11**(3), e0149804.

Wang, Q. X. (1998), 'The evolution of a gas bubble near an inclined wall', Theor. Comput. *Fluid Dyn*.**12**(1), 29–51.

Wang, Q. X. (2004), 'Numerical simulation of violent bubble motion', *Phys*. *Fluids* **16**(5), 1610–1619.

Wang, Q. X. (2014) Multi-oscillations of a bubble in a compressible liquid near a rigid boundary, J. Fluid Mech. 745, 509-536.

Wang Q.X. (2017) Oscillation of a bubble in a liquid confined in an elastic solid. Phys. Fluids, 29, 072101.

Wang, Q. X. (2016) Local energy of a bubble system and its loss due to acoustic radiation. Journal of Fluid Mech. 797, 201–230.

Wang, Q. X. and Blake, J. R. (2010) Nonspherical bubble dynamics in a compressible liquid. Part 1. Travelling acoustic wave. J. Fluid Mech. **659**, 191-224.

Wang, Q. X. and Blake J. R. (2011) Nonspherical bubble dynamics in a compressible liquid. Part 2. Acoustic standing wave. J. Fluid Mech. **679**, 559-581.

Wang, Q. X. & Manmi, K. (2014), 'Three dimensional microbubble dynamics near a wall subject to high intensity ultrasound', *Phys*. *Fluids* **26**(3), 032104.

Wang, Q. X., Manmi, K. & Calvisi, M. L. (2015), 'Numerical modeling of the 3D dynamics of ultrasound contrast agent microbubbles using the boundary integral method', *Phys*. *Fluids* **27**(2), 022104.

Wu, G. X. (1998), 'Hydrodynamic force on a rigid body during impact with liquid', *J. Fluid Struct*. **12**(5), 549–559.

Yamashita, T. Ando, K. (2019) Low-intensity ultrasound induced cavitation and streaming in oxygen-supersaturated water: Role of cavitation bubbles as physical cleaning agents. Ultrasonics Sonochemistry 52, 268-279.

Zhang, A. M. & Liu, Y. L. (2015), 'Improved three-dimensional bubble dynamics model based on boundary element method', *J. Comp. Phys*. **294**, 208–223.